

Aberystwyth University

Infrared Spectrometer for ExoMars: A Mast-Mounted Instrument for the Rover

Korablev, O. I.; Dobrolensky, Y.; Evdokimova, N.; Fedorova, A. A.; Kuzmin, V. O.; Mansevich, S. N.; Cloutis, E. A.; Carter, John; Poulet, F.; Flahaut, J.; Griffiths, A.; Gunn, Matthew; Schmitz, N.; Martín-Torres, J.; Zorzano, M. -P.; Rodionov, D. S.; Vago, J. L.; Stepanov, A. V.; Titanov, A. Y.; Vyazovetsky, N. A.

Published in:
Astrobiology

DOI:
[10.1089/ast.2016.1543](https://doi.org/10.1089/ast.2016.1543)

Publication date:
2017

Citation for published version (APA):

Korablev, O. I., Dobrolensky, Y., Evdokimova, N., Fedorova, A. A., Kuzmin, V. O., Mansevich, S. N., Cloutis, E. A., Carter, J., Poulet, F., Flahaut, J., Griffiths, A., Gunn, M., Schmitz, N., Martín-Torres, J., Zorzano, M. -P., Rodionov, D. S., Vago, J. L., Stepanov, A. V., Titanov, A. Y., ... Ivanov, A. Y. (2017). Infrared Spectrometer for ExoMars: A Mast-Mounted Instrument for the Rover. *Astrobiology*, 17(6-7), 542-564.
<https://doi.org/10.1089/ast.2016.1543>

General rights

Copyright and moral rights for the publications made accessible in the Aberystwyth Research Portal (the Institutional Repository) are retained by the authors and/or other copyright owners and it is a condition of accessing publications that users recognise and abide by the legal requirements associated with these rights.

- Users may download and print one copy of any publication from the Aberystwyth Research Portal for the purpose of private study or research.
- You may not further distribute the material or use it for any profit-making activity or commercial gain
- You may freely distribute the URL identifying the publication in the Aberystwyth Research Portal

Take down policy

If you believe that this document breaches copyright please contact us providing details, and we will remove access to the work immediately and investigate your claim.

tel: +44 1970 62 2400
email: is@aber.ac.uk

Astrobiology Manuscript Central: <http://mc.manuscriptcentral.com/astrobiology>**INFRARED SPECTROMETER FOR EXOMARS (ISEM), A MAST-MOUNTED INSTRUMENT FOR THE ROVER**

Journal:	<i>Astrobiology</i>
Manuscript ID	AST-2016-1543.R1
Manuscript Type:	Reviews
Date Submitted by the Author:	n/a
Complete List of Authors:	<p>Korablev, Oleg; Space Research Institute of the Russian Academy of Sciences (IKI)</p> <p>Dobrolensky, Yurii; Space Research Institute of the Russian Academy of Sciences (IKI)</p> <p>Evdokimova, Nadezhda; Space Research Institute of the Russian Academy of Sciences (IKI)</p> <p>Fedorova, Anna; Space Research Institute of the Russian Academy of Sciences (IKI)</p> <p>Kuzmin, Ruslan; Vernadsky Institute, Russian Academy of Sciences; Space Research Institute of the Russian Academy of Sciences (IKI)</p> <p>Mantsevich, Sergei; Lomonosov Moscow State University, Department of Physics; Space Research Institute of the Russian Academy of Sciences (IKI)</p> <p>Cloutis, Edward; University of Winnipeg, Geography</p> <p>Carter, John; Institut d'Astrophysique Spatiale</p> <p>Poulet, Francois; Institut d'Astrophysique Spatiale, CNRS/Université Paris-Sud,</p> <p>Flahaut, Jessica; Université Lyon 1, Ens de Lyon, CNRS</p> <p>Griffiths, Andrew; University College London Department of Space and Climate Physics</p> <p>Gunn, Matthew; Aberystwyth University, Institute of Mathematics & Physics</p> <p>Schmitz, Nicole; Deutsches Zentrum für Luft und Raumfahrt</p> <p>Martín-Torres, Javier; Luleå University of Technology, Division of Space Technology, Department of Computer Science, Electrical and Space Engineering; Instituto Andaluz de Ciencias de la Tierra (CSIC-UGR)</p> <p>Zorzano, Maria-Paz; Luleå University of Technology, Division of Space Technology, Department of Computer Science, Electrical and Space Engineering; Centro de Astrobiología (INTA-CSIC)</p> <p>Rodionov, Daniil; Space Research Institute of the Russian Academy of Sciences (IKI)</p> <p>Vago, Jorge; European Space Agency, SCI-S</p> <p>Stepanov, Alexander; Lomonosov Moscow State University, Department of Physics; Space Research Institute of the Russian Academy of Sciences (IKI)</p> <p>Titov, Andrei; Space Research Institute of the Russian Academy of Sciences (IKI)</p> <p>Vyazovetsky, Nikita; Space Research Institute of the Russian Academy of Sciences (IKI)</p>

1
2
3
4
5
6
7
8
9
10
11
12
13
14
15
16
17
18
19
20
21
22
23
24
25
26
27
28
29
30
31
32
33
34
35
36
37
38
39
40
41
42
43
44
45
46
47
48
49
50
51
52
53
54
55
56
57
58
59
60

	Trokhimovskiy, Alexander; Space Research Institute of the Russian Academy of Sciences (IKI) Sapgir, Alexander; Space Research Institute of the Russian Academy of Sciences (IKI) Kalinnikov, Yurii; 15National Research Institute for Physicotechnical and Radio Engineering Measurements VNIIFTRI Ivanov, Yurii; Main Astronomical Observatory National Academy of Sciences of Ukraine Shapkin, Alexei; Space Research Institute of the Russian Academy of Sciences (IKI) Ivanov, Andrei; Space Research Institute of the Russian Academy of Sciences (IKI)
Keyword:	Mars, Planetary Geology, Planetary Instrumentation, Planetary Habitability and Biosignatures, Spectroscopy
Manuscript Keywords (Search Terms):	ExoMars, ISEM, AOTF, infrared

SCHOLARONE™
Manuscripts

1
2
3
4
5
6
7 **1 INFRARED SPECTROMETER FOR EXOMARS (ISEM), A MAST-**
8 **2 MOUNTED INSTRUMENT FOR THE ROVER**
9

10
11 4 O.I. Korablev¹, Yu. Dobrolensky¹, N. Evdokimova¹, A.A. Fedorova¹, R.O.
12 5 Kuzmin^{2,1}, S.N. Mantsevich^{3,1}, E.A. Cloutis⁴, J. Carter⁵, F. Poulet⁵, J. Flahaut⁶, A.
13 6 Griffiths⁷, M. Gunn⁸, N. Schmitz⁹, J. Martín-Torres^{10,11}, M.-P. Zorzano^{10,12}, D.S.
14 7 Rodionov¹, J.L. Vago¹³, A.V. Stepanov^{3,1}, A.Yu. Titov¹, N.A. Vyazovetsky¹, A.Yu.
15 8 Trokhimovskiy¹, A.G. Sapgir¹, Yu. K. Kalinnikov¹⁴, Yu.S. Ivanov¹⁵, A.A.
16 9 Shapkin¹, A.Yu. Ivanov¹.

17
18
19
20
21 11 ¹Space Research Institute IKI, Moscow, Russia

22 12 ²Vernadsky Institute of Geochemistry and Analytical Chemistry GEOKHI,
23 13 Moscow, Russia

24 14 ³Department of Physics, Lomonosov Moscow State University, Russia

25 15 ⁴The University of Winnipeg, Winnipeg, Manitoba, Canada R3B 2E9

26 16 ⁵Institut d'Astrophysique Spatiale IAS-CNRS/Université Paris Sud, Orsay, France

27 17 ⁶Université Lyon 1, ENS-Lyon, CNRS, UMR 5276 LGL-TPE, F-69622,
28 18 Villeurbanne, France

29 19 ⁷Mullard Space Science Laboratory, University College London, UK

30 20 ⁸Department of Physics, Aberystwyth University, UK

31 21 ⁹German Aerospace Center DLR, Köln, Germany

32 22 ¹⁰Division of Space Technology, Department of Computer Science, Electrical and
33 23 Space Engineering, Luleå University of Technology, Kiruna, Sweden

34 24 ¹¹Instituto Andaluz de Ciencias de la Tierra (CSIC-UGR), Granada, Spain

35 25 ¹²Centro de Astrobiología (INTA-CSIC), Madrid, Spain

36 26 ¹³ESA ESTEC, Noordwijk, The Netherlands

37 27 ¹⁴National Research Institute for Physicotechnical and Radio Engineering
38 28 Measurements VNIIFTRI, Mendeleevo, Russia

39 29 ¹⁵Main Astronomical Observatory MAO NASU, Kyiv, Ukraine
40
41
42
43
44
45
46
47
48
49

50 **32 Abstract**

51 33 ISEM (Infrared Spectrometer for ExoMars) is a pencil-beam infrared
52 34 spectrometer that will measure reflected solar radiation in the near infrared range
53 35 for context assessment of the surface mineralogy in the vicinity of the ExoMars
54 36 rover. The instrument will be accommodated on the mast of the rover, and will be
55
56
57
58
59
60

1
2
3
4
5
6
7 37 operated together with the PanCam High-Resolution Camera (HRC). ISEM will
8 38 study the mineralogical and petrographic composition of the martian surface in
9 39 the vicinity of the rover, and in combination with the other remote sensing
10 40 instruments, aid the selection of potential targets for close-up investigations and
11 41 drilling sites. Of particular scientific interest are water-bearing minerals, such as
12 42 phyllosilicates, sulfates, carbonates, and minerals indicative of astrobiological
13 43 potential, such as borates, nitrates, and ammonium-bearing minerals. The
14 44 instrument has a $\sim 1^\circ$ field of view and covers the spectral range between 1.15–
15 45 3.30 μm with a spectral resolution varying from 3.3 nm at 1.15 μm to 28 nm at
16 46 3.30 μm . ISEM's optical head is mounted on the mast, and its electronics box is
17 47 located inside the rover's body. The spectrometer employs an acousto-optic
18 48 tunable filter (AOTF), and a Peltier-cooled InAs detector. The mass of ISEM is
19 49 1.74 kg, including the electronics and harness. The science objectives of the
20 50 experiment, the instrument design, and operational scenarios are described.
21
22
23
24
25
26
27

28 53 **1 Introduction**

29 54 The ExoMars rover is a mobile laboratory equipped with a drill to sample the
30 55 surface of Mars to a maximum depth of 2 m, and a suite of instruments to analyze
31 56 the samples. The drilling device is the only means to access near subsurface
32 57 materials and introduce them to the internal analytical laboratory. As the number
33 58 of samples obtained with the drill will be limited, the selection of high value sites
34 59 for drilling will be crucial. The rover's mast is therefore equipped with a set of
35 60 remote sensing instruments to assist the selection process by characterizing the
36 61 geological and compositional properties of the surrounding terrains. It includes
37 62 several cameras – a pair of navigation cameras (NavCam), and a panoramic
38 63 camera (PanCam). PanCam consists of stereo multispectral wide-angle camera
39 64 pair (the WACs) and a high-resolution color camera (HRC) (Coates et al, this
40 65 issue) and will provide the context images used to plan travelling and sampling.
41 66 To complement and enhance the capabilities of the remote sensing suit, an
42 67 infrared spectrometer able to unambiguously distinguish many rocks and minerals
43 68 from their spectral reflectance, will allow remote characterization and selection of
44 69 potential astrobiological targets. This mast-mounted IR spectrometer was
45 70 proposed during an early discussion of the new ESA-Roscosmos ExoMars
46 71 configuration as a useful addition to the rover science and to help operations by
47 72 characterizing from afar the mineralogical interest of targets that the rover could
48
49
50
51
52
53
54
55
56
57
58
59
60

1
2
3
4
5
6
7 73 visit.
8

9 74

10 75 ISEM is a derivative of the Lunar Infrared Spectrometer (LIS) (Korablev et al,
11 76 2015) being developed at the Space Research Institute (IKI) in Moscow for the
12 77 Luna-25 and Luna-27 Russian landers planned for flight in 2019 and 2021,
13 78 respectively (Zelenyi et al, 2014). Both the ISEM and LIS instruments have been
14 79 conceived with similar spectral capabilities. The ISEM design is improved with
15 80 respect to that of LIS, and modifications were also necessary to comply with the
16 81 more stringent environmental conditions on the ExoMars rover. A fully
17 82 operational model of ISEM is not ready at the moment of the paper submission,
18 83 and the assessment of its measurement performance has been made with the
19 84 available LIS prototype.
20
21
22
23

24 85

25 86 ISEM is one of two Roscosmos-provided instruments for the ExoMars Rover. It is
26 87 being predominantly developed at IKI, but includes contributions from the
27 88 National Research Institute for Physicotechnical and Radio Engineering
28 89 Measurements (VNIIFTRI) in Russia, Moscow State University, also in Russia,
29 90 and the Main Astrophysical Observatory, National Academy of Sciences in
30 91 Ukraine. A calibration target to be used jointly by PanCam and ISEM is being
31 92 contributed by Aberystwyth University, United Kingdom. Key components, such
32 93 as the AOTF and the detector, are purchased from NII Micropribor (Russia) and
33 94 Teledyne (USA). The science team includes researchers from Russia (IKI and
34 95 Vernadsky Institute), France, Italy, Sweden, Germany, UK, and Canada. The
35 96 team shares science team members with the PanCam and MicrOmega rover
36 97 instrument teams. A full list of the ISEM Science and Technical teams is given at
37 98 the end of the paper.
38
39
40
41
42

43 99

44 100 After a brief summary of the major objectives of the ExoMars mission, we
45 101 describe the scientific goals of the ISEM instrument. The technical design is then
46 102 detailed. Measured performances of LIS prototype and and expected
47 103 performances of ISEM are presented subsequently. We conclude the paper by
48 104 addressing the operational scenarios and related environmental constraints.
49
50

51 105

52 106 **2 Science Objectives**

53 107 **2.1 Contribution to overall rover mission science**

54 108 The scientific objectives of the ExoMars Program are defined as (Vago et al, this
55
56
57
58
59
60

109 issue):

- 110 1. To search for signs of past and present life on Mars;
- 111 2. To investigate the water/geochemical environment as a function of depth
112 in the shallow subsurface;
- 113 3. To study martian atmospheric trace gases and their sources;
- 114 4. To characterize the surface environment

115
116 The first two objectives are the most relevant to the ExoMars rover. The ISEM
117 experiment will contribute to achieving each of these objectives in the following
118 ways:

- 119 1. Many of the minerals and rocks detectable by ISEM are good indicators of
120 past habitable conditions, and of biological processes (e.g, carbonates,
121 oxalates, borates, nitrates, NH₄-bearing minerals (Applin et al, 2015; Berg
122 et al, 2016; Cloutis et al, 2016)) and may even contain biomolecules in
123 detectable concentrations. These include a class of biogenic minerals
124 which are further known to provide a substrate for, and catalyze pre-biotic
125 reactions. Organic compounds, including Polycyclic Aromatic
126 Hydrocarbons (PAHs) and those containing aliphatic C-H molecules, can
127 also be distinguished by ISEM (e.g, Clark et al, 2009; Izawa et al, 2014).
- 128 2. The ISEM instrument is capable of recognizing minerals and rocks, which
129 are indicative of the presence of water as well as geochemical
130 environmental indicators. ISEM can also be used to analyze the drill
131 cuttings excavated by the ExoMars drill system. The operating drill
132 obscures ISEM's view, and observing the cuttings is only possible after
133 the rover moves off and revisits the drilling site.
- 134 3. If present, ISEM could detect organic-bearing materials, possibly evolving
135 trace gases, such as hydrocarbons.
- 136 4. ISEM can carry out atmosphere observations, providing information on
137 dust and clouds, and contributing to characterization of the atmospheric
138 humidity. ISEM is capable of identifying and monitoring surface frost, and
139 may assess the diversity and stability of various minerals on the martian
140 surface, e.g, by monitoring changes in the spectral properties of drill
141 cuttings over time.

142
143 In terms of where the rover will land, ESA has issued the following scientific
144 criteria for landing site selection (Vago et al, 2015):

1
2
3
4
5
6
7 145

- 8 146 For the ExoMars Rover to achieve results regarding the possible existence of
9 147 biosignatures, the mission has to land in a **scientifically appropriate setting**:
10 148 1. The site must be **ancient** (older than 3.6 Ga) — from Mars' early, more
11 149 life-friendly period: the Noachian to the Noachian/Hesperian boundary;
12 150 2. The site must show abundant morphological and mineral evidence for
13 151 long-term, or frequently reoccurring, **aqueous activity**;
14 152 3. The site must include numerous **sedimentary outcrops**;
15 153 4. The outcrops must be **distributed** over the landing ellipse to ensure the
16 154 rover can get to some of them (typical rover traverse range is a few km);
17 155 5. The site must have **little dust** coverage.
18
19
20
21
22

23 157 ISEM addresses these criteria in the following ways:

- 24 158 1. The suite of samples that we have used to characterize ISEM in laboratory
25 159 tests includes materials similar to those found in Noachian terrains (e.g,
26 160 phyllosilicates, carbonates, etc.)
27 161 2. ISEM will be able to identify minerals that are indicative of aqueous
28 162 activity, such as phyllosilicates and hydrated sulfates.
29 163 3. Rocks and minerals presumed to have formed in sedimentary
30 164 environments are the main focus of our investigation and ISEM is
31 165 particularly well suited to detect and characterize them.
32 166 4. ISEM as a remote instrument is well adapted to characterize the
33 167 stratification at the outcrop scale.
34 168 5. Our investigation will assess the obscuring effects of dust, first of all on
35 169 the target areas, but also observing dust accumulation on the calibration
36 170 target, excavated drill cuttings (e.g, Rice et al, 2011).
37
38
39
40
41
42

43 172 **2.2. Synergies with other instruments**

44 173 The main goal of ISEM is to establish the mineral composition of Mars' surface
45 174 materials remotely. ISEM, together with PanCam (Fig. 1) offer high potential for
46 175 the remote identification and characterization of any scientifically high-value
47 176 targets in the vicinity of the rover, including proximal and distant rocks, outcrops,
48 177 and other geological formations. ISEM will help to establish the geological
49 178 context of each site along the rover traverse, discriminating between various
50 179 classes of minerals and rocks. ISEM will also be important in order to select
51 180 promising sites for subsurface sampling.
52
53
54
55
56
57
58
59
60

1
2
3
4
5
6
7 181

8 182 Infrared reflectance spectroscopy allows the study of the composition in the
9 183 uppermost few millimeters of a rock's surface. It allows discriminating between
10 184 various classes of silicates, (hydr-)oxides, hydrated/hydroxylated salts and
11 185 carbonates. As shown in Fig. 2, the 1.3° Field of View (FOV) of ISEM lies within
12 186 the 5° FOV of the color PanCam high-resolution camera (HRC), and they both
13 187 are within a much wider FOV (38.6°) of the Wide Angle Cameras (WACs) with
14 188 multispectral capabilities (Coates et al, this issue). The multispectral data are
15 189 produced using a filter wheel with 11 filter positions for each of the two WACs.
16 190 Out of the 22 filters, six are devoted to red, green, and blue broadband color,
17 191 duplicated in the both cameras, 12 are optimized for mineralogy in the 400-1000
18 192 nm range, and four "solar" filters are dedicated to atmospheric studies. By
19 193 extending the wavelength range beyond PanCam, ISEM will enable many more
20 194 spectral features diagnostic of specific mineralogy to be detected. Together
21 195 PanCam and ISEM provide spectrally resolved information from 0.4 to 3.3 μm.
22 196

23 196

24 197 The identification and mapping of the distribution of aqueous alteration products
25 198 in the upper surface layer, combined with subsurface data from the neutron
26 199 detector ADRON and the ground-penetrating radar WISDOM, will help to
27 200 understand the subsurface structure and the exobiology potential at each
28 201 prospective drilling site.
29 202

30 202

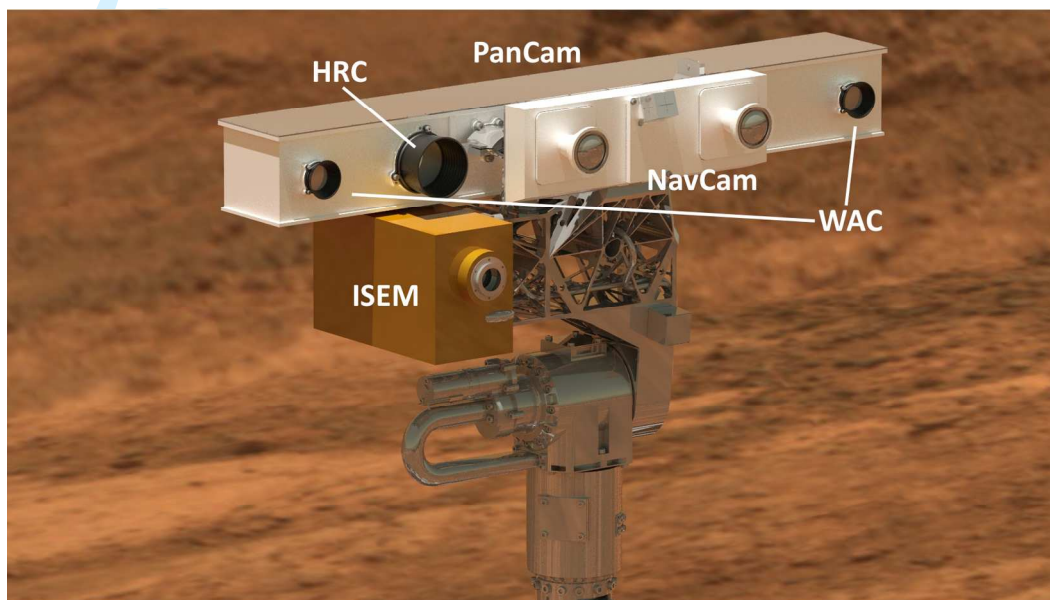
31 203 The collected drill samples will be analyzed in the rover's Analytical Laboratory
32 204 Drawer (ALD) by several instruments. The first is an infrared hyperspectral
33 205 microscope MicrOmega (Bibring et al, this issue). The principle of MicrOmega is
34 206 very similar to that of ISEM. The reflectance spectroscopy is performed in the
35 207 near-IR, but the analysis is done at the microscopic scale and the sample is
36 208 illuminated by monochromatic light source. In contrast to MicrOmega, ISEM has
37 209 a much wider field of view and range of detection. The distance to a target is not
38 210 really limited, and practically may reach hundreds of meters. Thus, ISEM is better
39 211 suited for accommodation on the rover mast, where it can be employed for target
40 212 identification of far away objects, but also for investigating outcrop, rock, and soil
41 213 mineralogy at close range.
42 214

43 214

44 215 There is no specific instrument dedicated to environmental characterization on the
45 216 rover. Although hampered by the limited number of observation cycles, ISEM,
46
47
48
49
50
51
52
53
54
55
56
57
58
59
60

217 jointly with PanCam, will deliver information regarding atmospheric aerosol
 218 opacity and the atmospheric gaseous composition. The data on water vapor
 219 content and aerosol will be retrieved as a by-product of reflectance spectra, from
 220 in-flight calibration, from the direct Sun imaging by PanCam, and from sky
 221 observations by PanCam and ISEM.

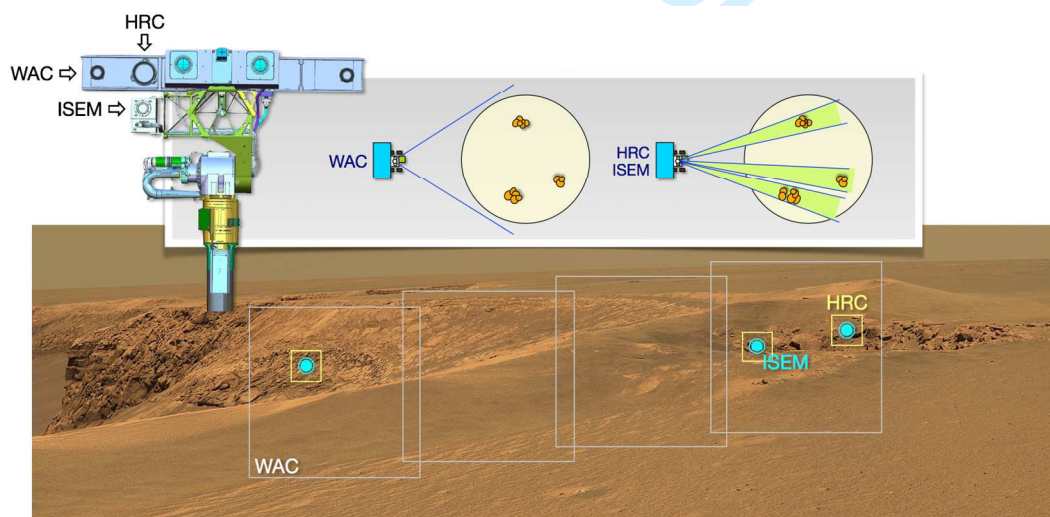
222



223

224 Figure 1. Schematic view of the ExoMars Rover mast instruments: PanCam,
 225 navigation cameras, and ISEM.

226



227

1
2
3
4
5
6
7 228 Figure 2. Schematic representation of possible ISEM and PanCam joint
8 229 observation scenario showing a sequence of ISEM measurements acquired
9 230 together with WAC and HRC PanCam frames.
10 231
11 232

12 233 **2.3 The method**

13 234 Near-IR spectroscopic observations of the Mars surface have not been performed
14 235 from any surface platform to date. Spectroscopy was employed on the Mars
15 236 Exploration Rovers (MER) in the thermal IR range (the radiation emitted by the
16 237 surface, 5-29 μm) with the Mini-TES instrument (Christensen et al, 2003,
17 238 2004a,b). These remote observations proved very useful for selecting targets for
18 239 *in situ* analyses by the Alpha Proton X-Ray Spectrometer (APXS) and Mossbauer
19 240 instruments on Spirit and Opportunity (e.g, Squyres et al, 2004). They also
20 241 allowed the identification of carbonates in Gusev Crater (Morris et al, 2010), and
21 242 undertook a number of atmospheric investigations (Smith et al, 2006).
22 243

23 244 Conversely, the near-IR spectral range (i.e. the infrared solar reflected radiation)
24 245 is being widely used in orbital observations, as it allows for significantly better
25 246 characterization of aqueous minerals than does the thermal infrared. To illustrate
26 247 this point, the TES instrument on Mars Global Surveyor (MGS) in the wavelength
27 248 range from 6 to 50 μm has mapped the distribution of both mafic and anhydrous
28 249 high-silica minerals (Bandfield et al, 2000; Christensen et al, 2001), but could not
29 250 unambiguously detect clay/clay-like minerals and salts, including carbonates. In
30 251 the near-IR, the OMEGA hyperspectral instrument on Mars Express (MEx)
31 252 measured the martian surface reflectance from 0.5 to 5.2 μm , and was able to
32 253 recognize a number of different phyllosilicates and sulfates (Bibring et al, 2006).
33 254 Building on OMEGA's success, the higher spatial resolution of the CRISM
34 255 instrument on Mars Reconnaissance Orbiter (MRO), which measures reflectance
35 256 from 0.362 to 3.92 μm , permitted the first detections of carbonates and serpentine
36 257 (Ehlmann et al, 2008, 2010). One shortcoming of the orbital observations is the
37 258 limited surface resolution (300-500 m per pixel for OMEGA/MEx and \sim 20 m for
38 259 CRISM/MRO), hindering the detection of small-scale exposures. In addition, such
39 260 instruments suffer from limited detection sensitivity owing to the combination of
40 261 the subtle nature of aqueous mineral spectroscopic features and to the short dwell
41 262 time of orbiting spacecraft. The wide variety of minerals on Mars detected by the
42 263 higher spatial resolution CRISM instrument compared to the lower resolution
43
44
45
46
47
48
49
50
51
52
53
54
55
56
57
58
59
60

1
2
3
4
5
6
7 264 OMEGA instrument demonstrates the greater mineralogical diversity that can be
8 265 identified as spatial resolution improves. Therefore the close-up near-IR
9 266 capability of ISEM on the ExoMars rover offers a very high diagnostic potential.
10 267

11 268 The small size and low mass of the ISEM instrument allows it to be
12 269 accommodated more easily on a rover platform. A similar AOTF-based near IR
13 270 spectrometer has been selected to enhance the capabilities of the successor to the
14 271 ChemCam instrument on the Curiosity Rover (Fouchet et al, 2015). The new
15 272 SuperCam instrument planned for the NASA 2020 rover utilizes a combination of
16 273 the Laser-Induced Breakdown Spectrometer (LIBS), Raman, and near-IR
17 274 reflectance spectroscopy, offering complementary elemental and mineralogical
18 275 analysis techniques.
19 276

20 277 Spectral range: An optimal spectral range for a near-IR mineralogical
21 278 characterization is 0.9-4.0 μm to encompass a broad absorption centered in the
22 279 0.95-1.1 μm region characteristic for pyroxene or olivine, and 3.4-3.9 μm for
23 280 carbonate overtones. The spectral range of the prototype LIS spectrometer is a
24 281 compromise of science requirements and technical limitations. Its longwave
25 282 bound of 3.3 μm allows for detection of hydration features in the 3 μm region
26 283 that can be used to discriminate different types of phyllosilicates and other
27 284 water/hydroxyl-bearing materials (e.g, Clark et al, 1990). The broad absorption in
28 285 the 3 μm region has contributions from the long wavelength wing of a hydroxyl
29 286 (OH) fundamental stretch usually centered near 2.7-2.8 μm , H₂O fundamental
30 287 stretches, and the first overtone of the H₂O bending fundamental (Clark et al,
31 288 1990). On Mars, hydration is strong enough that it can be detected at shorter
32 289 wavelengths. Clays and other hydrated minerals can be detected and
33 290 discriminated from overtones and combinations absorption features, at \sim 1.4 μm ,
34 291 \sim 1.9 μm , and 2.2-2.3 μm . Detection of carbonates by ISEM will be possible using
35 292 correlated 2.3- and 2.5- μm region bands, similar to CRISM/MRO (Ehlmann et al,
36 293 2008). Beyond 3.3-3.4 μm the signal is complicated by the thermal radiation of
37 294 the surface (and from the instrument itself, detectors with longer-wavelength
38 295 bound are much less sensitive because of thermal background). On the short
39 296 wavelength bound, the sensitivity of detectors optimized for 3- μm range falls
40 297 abruptly below 1 μm , hampering mafic silicate identification and characterization.
41 298 However mafic silicates can be recognized and discriminated by the shape of the
42 299 long wavelength wing of the 1- μm ferrous iron absorption band and the
43
44
45
46
47
48
49
50
51
52
53
54
55
56
57
58
59
60

1
2
3
4
5
6
7 300 wavelength position of the 2- μm ferrous iron absorption (see the following
8 301 section for the details).

9 302

10 303 Taking into account the advantages of the heritage design, we choose using the
11 304 same 1.15-3.3 μm range for ISEM on ExoMars as for the lunar instrument.

12 305

13 306 Spectral resolution. The spectral features of Mars surface materials will generally
14 307 include a mixture of several minerals, and are usually broad (>20 nm full width at
15 308 half maximum), so that there is no stringent requirement on the spectral resolution
16 309 for orbital instruments (see Table 1). With increasing spatial resolution, individual
17 310 minerals may become more apparent, with deeper characteristic absorption
18 311 features. Pure minerals can likely be observed only at the scale of individual
19 312 grains, e.g. with the microscope-spectrometer MicrOmega. Given that the ISEM
20 313 FOV will typically encompass an area of few cm^2 , a mixture of minerals will
21 314 likely be present, therefore a spectral resolution requirement of 25 cm^{-1} was
22 315 chosen that corresponds to 3.3 nm at 1.15 μm , 16 nm at 2.5 μm , and 28 nm at 3.3
23 316 μm .

24 317

25 318 In mineralogical studies, the best approach is the acquisition of the full available
26 319 spectral range. Nyquist sampling (two measured points per spectral resolution) of
27 320 the full 1.15-3.30 μm ($3030\text{-}8696 \text{ cm}^{-1}$) range with a spectral resolution of 25 cm^{-1}
28 321 results in 453 (512 with margin) spectral points. With a one-second exposure for
29 322 each spectral point, a complete spectrum is therefore measured in 8.5 minutes.
30 323 Customable or random wavelength access by the AOTF (see below) allows
31 324 oversampling, selecting different portions of the spectrum, and focusing on the
32 325 most interesting or diagnostic spectral intervals.

33 326

34 327 The color and IR reflectance of the Mars surface are what one would expect of
35 328 iron-bearing mineral species that are either primary or formed by hydrous or
36 329 anhydrous chemical weathering. The infrared reflectance varies from 5% to 35%,
37 330 with typical values being 15-20% for low albedo regions and 25-30% for high-
38 331 albedo regions (Erard 2001). A characteristic feature of Mars spectra is a deep
39 332 absorption feature starting beyond the 2.7- μm CO_2 saturated atmospheric band.
40 333 Its depth reflects the degree of hydration of the martian surface. An increase in
41 334 measured reflectance toward longer wavelengths signifies an increasing
42 335 contribution from emitted thermal radiation. Observations from the ExoMars

336 rover mast will be carried out using a broad range of phase angles, preferably at
 337 high Sun. There is no Sun avoidance requirement for ISEM.

338

339 Table 1. Near-IR spectrometers used and planned to study Mars surface

Instrument	Spectral range, μm	Spectral resolution, nm	Surface resolution	Ref.
ISM/Phobos 2	0.8 -3.1	50	20x30 km	Bibring et al, 1990
OMEGA/MEx	0.35-1 1-2.5 2.5-5.1	7 14 20	0.3-5 km	Bibring et al, 2004
CRISM/MRO	0.362-3.92	6.6/pix	18 m	Murchie et al, 2007
ISEM/ExoMars	1.1-3.3	3.3 at 1.15 μm 16 at 2.5 μm 28 at 3.3 μm	3-10 cm	This study
MicrOmega/ExoMars	0.5-3.65	2 at 1.0 μm 25 at 3.6 μm	20 μm	Bibring et al, this issue
SuperCam/2020 Rover	1.3-2.6	5 at 1.3 μm , 20 at 2.6 μm	1.3-7 mm	Fouchet et al, 2015

340

341

342 **2.4 Potentially detectable mineral groups**

343 The greatest share of what we know about martian mineralogy has been gleaned
 344 from orbital near- and thermal-infrared spectroscopy measurements. The infrared
 345 instruments have been successful in identifying igneous minerals, while the near-
 346 IR instruments were more important for detecting ancient hydrated minerals, such
 347 as phyllosilicates, as well as carbonates and sulfates, which could be used to
 348 develop a timeline of changing environmental conditions on Mars and evidence of
 349 previous more clement epochs on Mars. The capabilities of ISEM can be gauged
 350 against these detections to assess its expected science return, as well as
 351 expectations for detecting other mineral species of high scientific value, all in the
 352 context of the proposed ExoMars landing sites.

353

354 1. Phyllosilicates: The identification of hydrated phyllosilicates on the martian
 355 surface is one of the discoveries driving *in situ* exploration of Mars.

1
2
3
4
5
6
7 356 Phyllosilicates are commonly detected in ancient, Noachian-aged martian terrains
8 357 (Poulet et al, 2005). Various types of phyllosilicates have been observed,
9 358 including Fe/Mg and Al-rich smectites, micas, vermiculites, kaolinite, chlorite,
10 359 and serpentine (Ehlmann et al, 2009; Murchie et al, 2009; Carter et al, 2013). The
11 360 presence of these minerals likely indicates that conditions in the past were
12 361 favorable for the presence of liquid water at or near the surface. They are
13 362 considered good reaction templates for organic molecules and excellent for
14 363 biosignature preservation (Bishop et al, 2013, and references therein).
15
16 364 Phyllosilicates have been detected from orbit within the ellipse of two out of the
17 365 three candidate landing sites for the ExoMars rover, Oxia Planum and Mawrth
18 366 Vallis (Vago et al, this issue). They have not been detected in Aram Dorsum yet;
19 367 even if they are there, it may be difficult to see them from orbit. ISEM will have
20 368 the capabilities to detect sharp features between 1.35 and 2.6 μm in phyllosilicate
21 369 reflectance spectra, which are related to combinations and overtones of OH-M
22 370 stretching and bending bound to various cations (M) as well as the H-O-H stretch
23 371 and bend from water bound in interlayer regions or adsorbed on mineral surfaces
24 372 (Clark et al, 1990) (Figures 3a, b, and c).
25
26
27
28
29
30

31 374 2. Carbonates have been discovered on Mars at a number of locations from orbit
32 375 (Ehlmann et al, 2008, Wray et al, 2016), by surface rovers (Morris et al, 2010),
33 376 and in martian meteorites (e.g, McKay et al, 1996). The precise species are not
34 377 always known, but various Mg-Fe-Ca carbonates provide the best match for
35 378 observed spectral features. Carbonates are important minerals for identification as
36 379 they often indicate the presence of habitable (circum-neutral) environments. They
37 380 are also widely implicated in explaining the loss of a substantial fraction of the
38 381 presumed early Mars dense carbon dioxide atmosphere. Carbonate detection and
39 382 characterization is possible in a number of wavelength regions. The 2.2-2.6 μm
40 383 region is one of the best because it is not affected by thermal emission, and
41 384 absorption bands in this region vary in their positions for different carbonate
42 385 species (Figure 3d). ISEM may also be able to identify Fe-bearing from Fe-free
43 386 carbonates on the basis of the presence or absence of a ferrous iron absorption
44 387 band near 1.2 μm .
45
46
47
48
49
50

51 389 3. Sulfates: A number of sulfate minerals have been observed on Mars, both from
52 390 orbit and in situ, including poorly ($\leq 2 \text{ H}_2\text{O}$) hydrated species (gypsum, kieserite,
53 391 bassanite), and polyhydrated varieties (Squyres et al, 2004; Gendrin et al, 2005;
54
55
56
57
58
59
60

1
2
3
4
5
6
7 392 Wang et al, 2006; Flahaut et al, 2014; Nachon et al, 2014) as well as hydroxylated
8 393 species (copiapite, jarosite, alunite and the dehydrated form of amarantite
9 394 $\text{FeSO}_4(\text{OH})$). These sulfates are all water/hydroxyl-bearing and several are also
10 395 indicative of circum-neutral, perhaps habitable environments. Sulfates also have
11 396 the potential to preserve microfossils (e.g, Allwood et al, 2013) and concentrate
12 397 organic compounds (Noe Dobrea et al, 2016). Specific sulfates can be powerful
13 398 indicators of environmental conditions on Mars, past and present (e.g, Leftwich et
14 399 al, 2013). Sulfate discrimination is possible using a number of wavelength
15 400 intervals in the ISEM range. For example, gypsum is characterized by a uniquely-
16 401 shaped absorption band in the 1.4- μm region, jarosite and alunite by absorption
17 402 bands in the 1.8- μm region, and other sulfates by S-O associated absorption bands
18 403 in the 2.0-2.5 μm region (Cloutis et al, 2006) (Figures 3e and f).
19 404

20 405 4. Silica: Silica, in a variety of forms, is present in a number of terrains on Mars
21 406 (Bandfield et al, 2004; Smith and Bandfield, 2012; Smith et al, 2013, Carter et al,
22 407 2013). Differences in reflectance spectra can be used to distinguish different
23 408 forms of silica, some of which are associated with habitability (Rice et al, 2013).
24 409 The region most useful for distinguishing different forms of silica is located near
25 410 2.2 μm and is due to Si-OH overtones. The nature and abundance of these bonds
26 411 varies among different types of silica (Rice et al, 2013). This diagnostic feature
27 412 can be clearly seen in the reflectance spectra of two different grain sizes of quartz
28 413 (Figure 3g).
29 414

30 415 5. Igneous minerals. Petrologic investigations of martian rocks have been
31 416 accomplished by mineralogical, geochemical, and textural analyses by remote
32 417 sensing observations, in situ investigations, and laboratory analyses of martian
33 418 meteorites. Igneous rocks are found in numerous settings; NIR spectroscopy from
34 419 orbiting spacecraft has been an effective mineralogic tool to identify and to map
35 420 at a global scale various rock-forming minerals such as olivines, pyroxenes and
36 421 iron-bearing plagioclases (Poulet et al. 2009; Ody et al. 2013; Carter and Poulet
37 422 2013). (Figure 3h and i).
38 423

39 424 6. Ferrous oxides/hydroxides. These minerals are the widespread weathering
40 425 products of primary iron-bearing materials (Ody et al, 2012). In the ISEM spectral
41 426 range, they manifest themselves mainly in the shape of the continuum.
42 427 Hydroxides exhibit shallow absorption features, including near 1.41 and 1.93 μm ,
43
44
45
46
47
48
49
50
51
52
53
54
55
56
57
58
59
60

1
2
3
4
5
6
7 428 and several species have been reported from NIR orbital investigations. Some
8 429 iron-bearing species, such as goethite, exhibit Fe-OH absorption bands longward
9 430 of the same band in Fe-free minerals (Beck et al, 2011) (Figure 3j).

10 431

11 432 Several other potential candidates that are amenable to detection and analysis by
12 433 ISEM, and are of high scientific value, are described below.

13 434

14 435 Organic compounds –PAHs. Infrared spectroscopy is potentially sensitive to the
15 436 presence of organic compounds, which have already been identified *in situ*,
16 437 though in trace quantities, within Mars samples (Freissinet et al, 2015). PAHs are
17 438 generally a stable form of organic molecules, and if organic compounds are or
18 439 were present on the surface of Mars, they have likely transformed to PAHs
19 440 (Anders et al, 1996). PAHs are also the dominant form of organic material in
20 441 Archaean terrestrial rocks (Marshall et al, 2007; and references therein). Their
21 442 reflectance spectra exhibit absorption features that are largely associated with a
22 443 number of functional groups that may be present, particularly aliphatic C-H
23 444 molecules (Izawa et al, 2014). They can exhibit absorption bands near 1.69 μm
24 445 due to CH overtones, 1.50 μm due to N-H stretching overtones, and numerous
25 446 other overtone and combination bands beyond 2.1 μm . A shoulder of the
26 447 fundamental 3.2-3.35 μm aromatic band could be also detectable in the spectra,
27 448 though complicated by a deep 3- μm absorption, characteristic for Mars
28 449 reflectance in general, see below.

29 450

30 451 Perchlorates and chlorides. Perchlorates are strongly suspected to be present on
31 452 Mars on the basis of analytical results from the Phoenix lander in the polar region
32 453 (Hecht et al, 2009; Cull et al, 2010) and from the MSL Curiosity rover in the near-
33 454 equatorial region (Farley et al, 2016). Perchlorates have been linked both to the
34 455 destruction of organic compounds, and to liquid water. They can absorb
35 456 atmospheric water and allow for the existence of stable liquid water brines
36 457 (Martin-Torres et al, 2015). Their spectral properties have been the focus of
37 458 multiple studies (Bishop et al, 2014; Hanley et al, 2015) since the presence of
38 459 perchlorates could have strong implications for the (non) preservation of
39 460 biosignatures. Reflectance spectra are characterized by possible Cl-O-H₂O-
40 461 associated absorption bands near 1.35, 1.75, and 2.15 μm . The 3-micron signature
41 462 of water is present in IR spectra of perchlorate samples in the form of hydrate, ice
42 463 or liquid brine (Zorzano et al, 2009). Spectral features in a more suitable NIR

1
2
3
4
5
6
7 464 range have possibly been detected from orbit (Ojha et al, 2015), the efforts to
8 465 confirm this are under way. While anhydrous chloride salts are mostly featureless
9 466 in the wavelength range of ISEM, chlorinated species have been detected in
10 467 abundance at Mars (Osterloo et al, 2010), and their hydrated forms would be
11 468 detectable in the NIR (Hanley et al, 2011).
12
13

14
15 470 Oxalates. Oxalates are carbon-bearing minerals that new evidence suggests may
16 471 be present on Mars in addition to, or instead of, carbonates (Applin et al, 2015).
17 472 Terrestrial oxalates are typically formed in biological processes (Applin et al,
18 473 2016, and references therein). Their presence on Mars would suggest past
19 474 habitability and possibly biological processes. Oxalates have some similarities
20 475 with carbonates in terms of multiple C-O associated absorption bands, but their
21 476 wavelength positions and shapes differ from carbonates and can be used to
22 477 discriminate different oxalate species. Major oxalate absorption bands are present
23 478 in the 2.2-2.5 and 3.2-3.3 μm regions.
24
25
26
27

28 480 Water ice. The presence of water ice at the landing site during daytime
29 481 observations is unlikely, but cannot be excluded (Carrozzo et al, 2009). Seasonal
30 482 frost, if present at the landing site, will be readily identifiable by ISEM, allowing
31 483 study of its season deposition cycle and dependence on local conditions.
32 484 Unambiguous signatures of water ice are present in the ISEM wavelength range
33 485 with diagnostic absorption bands at 1.25, 1.5, 2.0 and 3.0 μm .
34
35
36
37

38 487 Nitrates. Nitrates may have been detected *in situ* on Mars (Navarro-Gonzalez et al,
39 488 2013). They are important minerals because they may indicate the operation of
40 489 biological processes and/or can serve as a bioavailable source of nitrogen. Their
41 490 spectral reflectance properties have recently been studied (Cloutis et al, 2016).
42 491 The NO_3 molecule gives rise to multiple absorption bands that can be detected
43 492 down to as low as 1.8 μm .
44
45
46
47

48 494 Phosphates. Phosphates are important as a potential indicator of biological
49 495 processes. They are a likely possibility to explain phosphorus, which has been
50 496 detected on Mars (Blake et al, 2013), but its form is not yet determined. Their
51 497 spectral properties are only partially known (Lane et al, 2011). They share some
52 498 similarities with some other mineral groups, including ferrous iron-associated
53 499 absorption bands in the 1- μm region and weak P-O absorption bands in the 2-2.5
54
55
56
57
58
59
60

1
2
3
4
5
6 500 μm region. Robust phosphate detection by ISEM may not be feasible.
7

8 501

9 Borates. Borates are another important mineral group that can be associated with
10 habitability and biological processes (Stephenson et al, 2013). Boron cannot be
11 detected with an APXS instrument (Cloutis et al, 2016), but it has been detected
12 504 detected with an APXS instrument (Cloutis et al, 2016), but it has been detected
13 505 and quantified in clays from martian meteorite MIL090030 (Stephenson et al,
14 506 2013). Borate deposits on Earth are often associated with enclosed evaporitic
15 507 deposits and might be present in association with martian chlorides and sulfate
16 508 salts. Borates exhibit B-O associated absorption bands in the 1.55, and 2.15-2.25
17 509 μm regions, enabling their detection using multiple wavelength intervals and
20 510 absorption features measurable by ISEM. Absorption band positions and shapes
21 511 vary between different borates.
22

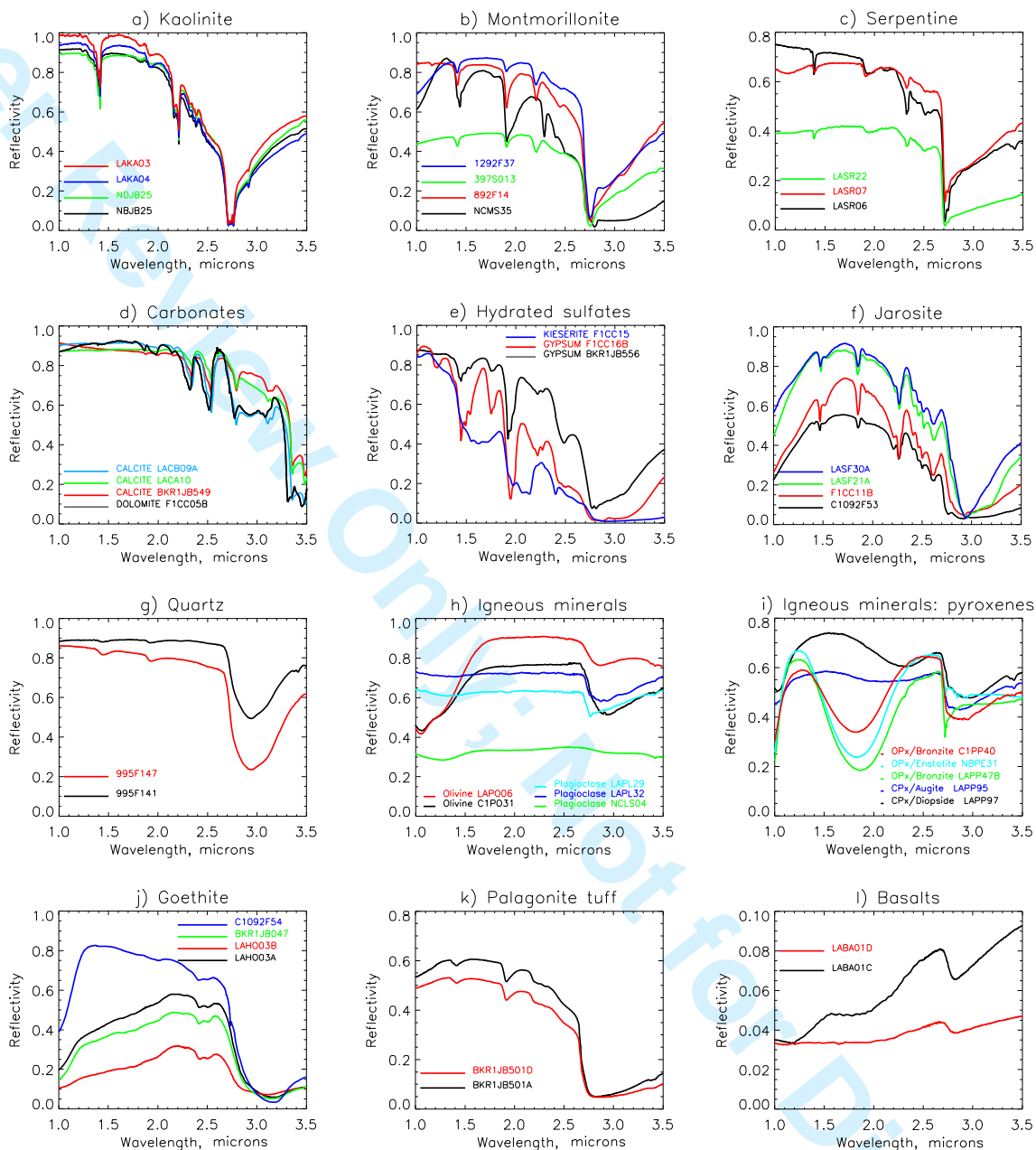
23 512

24 513 Ammonium-bearing minerals. The presence of the ammonium (NH_4) molecule in
25 514 various minerals leads to strong absorption bands in the 1.6, 2.0-2.2 and 3.1 μm
26 515 regions. Band shapes and positions can be used to discriminate different
27 516 ammonium-bearing minerals (Berg et al, 2016). Ammonium-bearing minerals are
28 517 of astrobiological importance for a number of reasons. Ammonium is often of
29 518 biological origin, has high thermal stability, and can withstand some level of
30 519 metamorphism (Boyd, 2001). Ammonium-bearing minerals on Mars have
31 520 possibly been detected from spectroscopic observations made from orbit (Sefton-
32 521 Nash et al, 2012), and a nitrogen cycle on Mars has been suggested to operate
33 522 (Manning et al, 2008). Low concentrations of ammonium in soil have been
34 523 reported for the Phoenix landing site (Quinn et al, 2011).
35 524

36 525

37 526 One of the limitations of spectrally characterizing Mars-relevant minerals with
38 527 ISEM under ambient terrestrial conditions is that these mineral spectra display a
39 528 nearly ubiquitous broad and frequently deep absorption feature in the 3- μm region.
40 529 This is normally attributable to water that may be present in various forms,
41 530 including adsorbed, fluid inclusions, impurities or accessory phases, or due to
42 531 incipient alteration. This feature is normally seen even in nominally anhydrous
43 532 minerals, such as olivine and pyroxene (see Figure 3h and i; more examples of
44 533 Mars background material spectra are presented in Figure 3 j, k, and l). When
45 534 such minerals are exposed to Mars-like surface conditions, the 3- μm feature
46 535 commonly shows a reduction in both depth and width, but rarely disappears
47 completely (Cloutis et al, 2007; Cloutis et al, 2008). It may be possible to use
48
49
50
51
52
53
54
55
56
57
58
59
60

1
2
3
4
5
6
7 536 characteristics of the 3- μ m absorption feature to constrain or determine water
8 537 content (Milliken and Mustard, 2005), but in multicomponent targets, such
9 538 determinations will be more difficult. Small amounts of water in the near
10 539 subsurface and on the surface of Mars also seems to be ubiquitous, displaying
11 540 seasonal variations (Milliken et al, 2007). Collectively these results suggest that
12 541 the 3- μ m region may not be best suited for mineralogical determinations using
13 542 ISEM. However, as discussed above, other wavelength regions accessible to
14 543 ISEM have significant diagnostic potential for a wide range of minerals, as
15 544 demonstrated effusively from terrestrial and Mars orbital studies.
16
17
18
19
20
21
22
23
24
25
26
27
28
29
30
31
32
33
34
35
36
37
38
39
40
41
42
43
44
45
46
47
48
49
50
51
52
53
54
55
56
57
58
59
60



548

549

550

551

552

553

554

555

556

557

558

559

560

Figure 3. Example spectra of minerals and rocks in the ISEM spectral range, which may be expected at the ExoMars landing sites (from CRISM spectral library, http://pds-geosciences.wustl.edu/missions/mro/spectral_library.htm; sample labels from this library). The upper half of the figure (a-f) shows the spectra of minerals the most significant for habitability, while the spectra shown

1
2
3
4
5
6
7 554 in the lower half (g-i) are more relevant to background minerals and dust. The
8 555 spectral resolution of CRISM is close to that of ISEM in the center of the range;
9 556 ISEM resolution is better at shorter wavelengths, and coarser at 3 μm (see Table
10 557 1).
11 558

13 559 **2.5 Atmospheric studies (aerosol, gaseous content)**

14 560 There is no dedicated instrument, such as e.g. meteorological station on the
15 561 ExoMars rover to characterize the environmental conditions. Therefore any
16 562 information available by other means is of particular value. Spectrally resolved
17 563 data in the visible-NIR and in the thermal IR ranges have been used to assess the
18 564 atmospheric state from Mars Pathfinder and Mars Exploration Rovers. In the
19 565 spectral range of ISEM there are absorption bands of atmospheric CO_2 (at 1.43,
20 566 1.6, 2.0, and 2.7 μm) and H_2O (at 1.38 and 2.56 μm), and it is well suited, in
21 567 particular its short-wave sub-range to characterize the main mode of the martian
22 568 dust (Fedorova et al, 2014). The condensation clouds in the equatorial region
23 569 consist predominantly of water ice (Vincendon et al, 2011), with multiple
24 570 absorption bands within the ISEM spectral range (see section 2.4). Carbon
25 571 dioxide clouds if present at high altitudes may be detected by distinct features of
26 572 solid CO_2 near 1.2, 1.4, 1.5, 2.0, 2.7, and 3.0 μm .
27 573

28 574 The gaseous absorptions will be measured by ISEM as a by-product of every
29 575 surface measurement. Depth of the CO_2 absorptions can be used to determine the
30 576 surface pressure, and the H_2O absorptions quantify the total column water
31 577 contents in the atmosphere above the site. To disentangle the possible overlapping
32 578 atmospheric and mineral features in the reflected surface spectra, preferentially
33 579 the observations of the *in situ* calibration target will be interpreted. The estimate
34 580 of accuracy to retrieve the atmospheric pressure by ISEM is given by OMEGA
35 581 study of the 2- μm CO_2 absorption from the orbit: 7-10 Pa (~1%) 1-sigma. (Forget
36 582 et al, 2007). With the optical path being half of the OMEGA case, our retrieval
37 583 accuracy will be comparable.
38 584

39 585 More precise measurements of surface pressure, minor gases, and better
40 586 characterization of the atmospheric dust and cloud situation by ISEM will be
41 587 possible using dedicated atmospheric observations. They will be coordinated with
42 588 those by PanCam. The PanCam atmospheric study (Coates et al, this issue) will
43 589 include direct solar observations just prior to sunset (to take advantage of the
44
45
46
47
48
49
50
51
52
53
54
55
56
57
58
59
60

1
2
3
4
5
6
7 590 maximal atmospheric path lengths) and cross sky brightness measurements. Such
8 591 observations, e.g. performed with Mars Pathfinder camera (Titov et al, 1999;
9 592 Markiewicz et al, 1999) or MERs (Lemmon et al, 2004; Smith et al, 2006) can be
10 593 significantly strengthened by extending the spectral range to the near-IR.
11 594

12 595 Direct solar observations by ISEM are not so far in the baseline. Their
13 596 implementation would allow for high-accuracy pressure and water retrievals,
14 597 better optical characterization of dust, direct and localized detection of H₂O ice
15 598 and, if present, the CO₂ ice clouds. Observing the Sun at different zenith angles
16 599 helps putting constraints on the vertical distribution of water vapor. However
17 600 ISEM is optimized for weak reflected light, and measuring the direct Sun signal
18 601 may not be feasible. We successfully tested this possibility with the lunar
19 602 prototype, but the ISEM aperture is larger, and a solar-blind filter within the
20 603 foreoptics might become necessary. Such a filter would cause a several percent
21 604 signal loss for the baseline ISEM observations. A final assessment of the direct
22 605 Sun mode will be done during the characterization of the flight model.
23 606

24 607 The cross-sky brightness measurements by ISEM are the best suited for
25 608 characterizing the aerosol component of the Mars atmosphere. Because of quasi-
26 609 permanent aerosol loading, the brightness of the martian sky at low zenith angles
27 610 is not significantly lower than that from light scattered from the surface.
28 611 Measurements at a range of phase angles will allow to extract the size distribution,
29 612 optical properties, and even to assess the shape of aerosols suspended in the
30 613 atmosphere. Water vapor absorption at 2.56 μm is much stronger than that at 0.94
31 614 μm to be observed by WAC in solar filters, and the ISEM data might put
32 615 additional constraints on the vertical distribution of water in the boundary layer of
33 616 atmosphere.
34 617

35 618 The variety of atmospheric measurements by ISEM calibrated using an *in situ*
36 619 calibration target will allow the refinement of atmospheric scattering models and
37 620 therefore refinement of the calibration of orbital spectral measurements of the
38 621 martian surface.
39 622

40 623 **3 Instrument Description**

41 624 **3.1 Instrument concept**

42 625 The measurement principle of ISEM is based on the use of an AOTF. The core
43
44
45
46
47
48
49
50
51
52
53
54
55
56
57
58
59
60

1
2
3
4
5
6
7 626 element of an AOTF is a birefringent crystal (typically of paratellurite, TeO_2 , due
8 627 to the combination of acoustic and optical properties) with a welded
9 628 piezotransducer. The radio frequency (RF) applied to the transducer generates an
10 629 acoustic field in the crystal, implementing acousto-optic interactions in Bragg's
11 630 regime. The spectral selectivity of the acousto-optic diffraction allows the
12 631 filtering of light. The diffraction occurs for a single wavelength, and there are no
13 632 diffraction orders. The applied RF controls the tuning of the AOTF. AOTFs are
14 633 technologically mature and widely used for spectral analysis. The robust design,
15 634 small dimensions and mass, coupled to the absence of moving parts in an AOTF-
16 635 based spectrometer, makes them popular for space applications. So far AOTF-
17 636 based spectrometers have been used in space science: (i) to study the atmospheric
18 637 composition of Mars and Venus (Korablev et al, 2006, 2012); (ii) on the Moon
19 638 within the Chang'e-3 VNIS spectrometer (0.45-2.4 μm) mounted on the Yutu
20 639 rover (He et al, 2014); (iii) for isolation of echelle-spectrometer diffraction orders
21 640 in high-resolution instruments (Nevejans et al, 2006; Korablev et al, 2011, 2014;
22 641 Neefs et al, 2015); and (iv) to illuminate the sample of an IR microscope with
23 642 monochromatic light (Pilorget and Bibring 2013).
24
25
26
27
28
29
30

31 644 Wider application of the AOTFs in remote sensing is hampered by the inherent
32 645 requirement to sequentially scan the spectrum. On an orbital mission with a short
33 646 dwell time, this scanning interferes with the spacecraft or line of sight motion,
34 647 complicating the analysis. Even for a pencil-beam device, different parts of the
35 648 acquired spectrum would correspond to different observed areas. Conversely,
36 649 observations from a static point, such as a planetary lander, or a rover, which
37 650 remains immobile during the measurement, are well suited for AOTF-based
38 651 instruments.
39
40
41
42

43 653 As described in the Introduction, ISEM is a close equivalent of LIS being
44 654 developed for two Russian lunar landers. The LIS development is more advanced
45 655 with respect to that of ISEM — by about two years. LIS benefited from the
46 656 experience gained from the pencil-beam spectrometer design of the Mars Express
47 657 and Venus Express instruments, and from the early developments of MicrOmega.
48 658 SPICAM-IR AOTF spectrometer with the spectral range 0.9-1.7 μm (Korablev et
49 659 al, 2006) has been operating in Mars orbit since 2004. A similar SPICAV-IR
50 660 instrument employing a double-range AOTF operated in Venus orbit from 2006
51 661 to 2014 (Korablev et al, 2012). A double-range AOTF for the spectral range of
52
53
54
55
56
57
58
59
60

662 0.7-4.1 μm serving as a prototype to the LIS and ISEM's AOTFs was developed
 663 for the Phobos Grunt mission (Leroi et al, 2009).

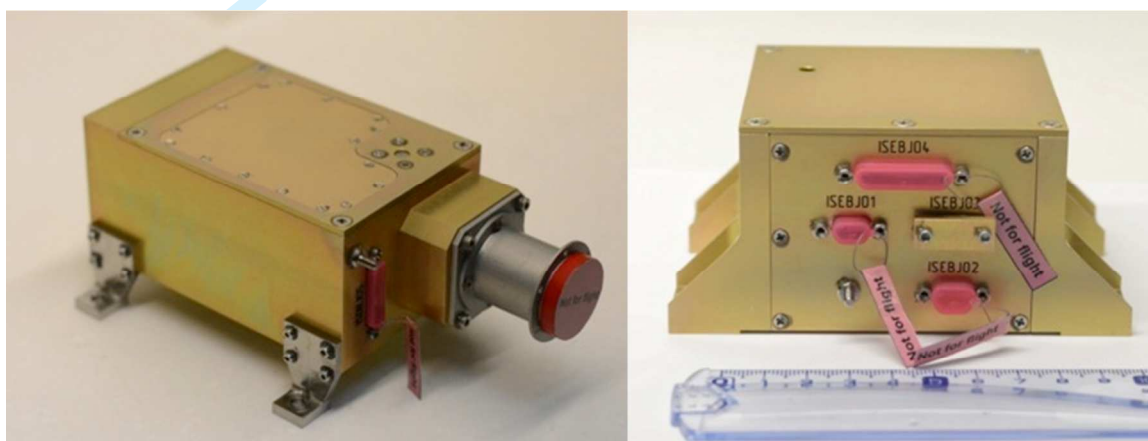
664

665 In order to reduce the influence of the extreme temperature conditions at the
 666 rover's mast on the electronics, the instrument is implemented as two separate
 667 boxes, a mast-mounted Optical Box (OB) and the Electronics Box (EB) (Fig. 4).

668 The thermally stabilized EB is mounted within the rover's body.

669

670



671

672 Figure 4. The ISEM instrument, the photographs of the optical and electronics
 673 box structural and thermal models.

674

675

676 Table 1. ISEM main characteristics and resources

Parameter	Value
Spectral range	1.15-3.3 μm
Spectral resolution	better than 25 cm^{-1} 3.3 nm at 1.15 μm , 16 nm at 2.5 μm , 28 nm at 3.3 μm
FOV	1.3°
Temperature range, operational	-45°C...+30°C (Optical box, OB) -40°C...+50°C (Electronics box, EB)
Temperature range, non-operational	-60°...+60°C (OB and EB) -130°...+60°C for OB pending final confirmation
AOTF	
Material	TeO ₂
Spectral range	1.15-3.39 μm

Parameter	Value
Effectiveness	>50 % (in polarized light)
Aperture	Ø 5 mm, 5°×5°;
Mean RF power	5 W
RF frequency range	23-82 MHz
Detector	InAs photodiode, Ø1 mm, 1-3.45 µm Teledyne Judson Technologies J12TE3-66D-R01M, 3-stage Peltier cooler
ADC	16-bit
Number of points per spectral range	variable, by default 1024 for one observation
Data volume	variable, by default 20 Kbit for one observation
Data/command interface	RS-422
Powers supply voltage	28 V
Power consumption, W	
Peak	14
Average	11.5
Standby	9
Dimensions	160×80×96 mm OB 116×84×55 mm EB
Mass, overall	1.740 kg
OB	0.690 kg
EB	0.560 kg
Calibration target (ISEM part)	0.014 kg
Harness	0.476 kg including 20% margin (TAS-I data)

677

678

679

680 3.1 The Optical Box

681 Though most of the electronics are in the EB, some electronics such as the

682 detector's preamplifier, and the RF conditioning electronics remain in the OB.

683 Neither the weak photodiode current, nor the power RF can be transmitted via the

684 5-m harness. The block-diagram of ISEM is presented in Fig. 5.

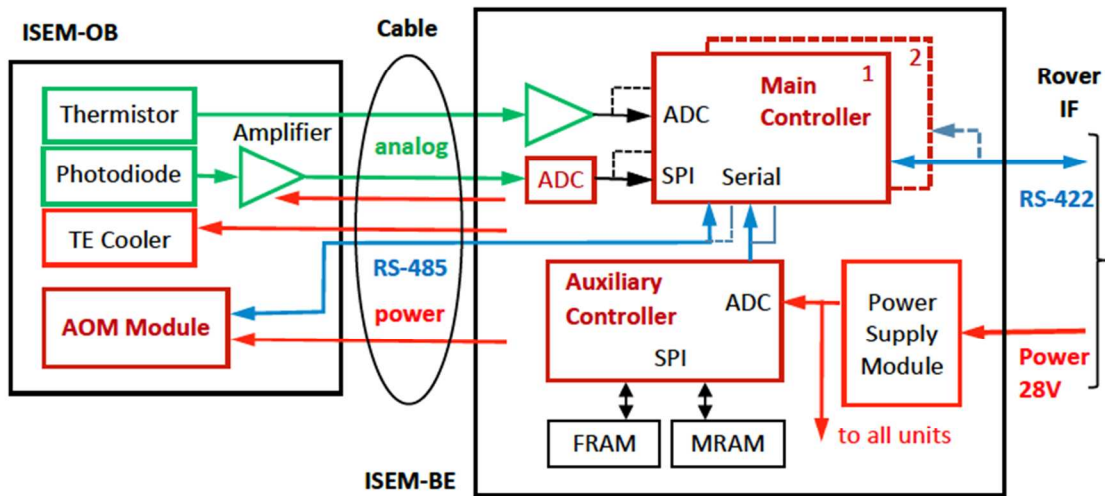
685

686 The OB contains all the optical elements, the AOTF with associated electronics

687 (ultrasound frequency synthesizer and amplifier boards), the photo detector and

688 the photo detector board (Fig. 6).

689

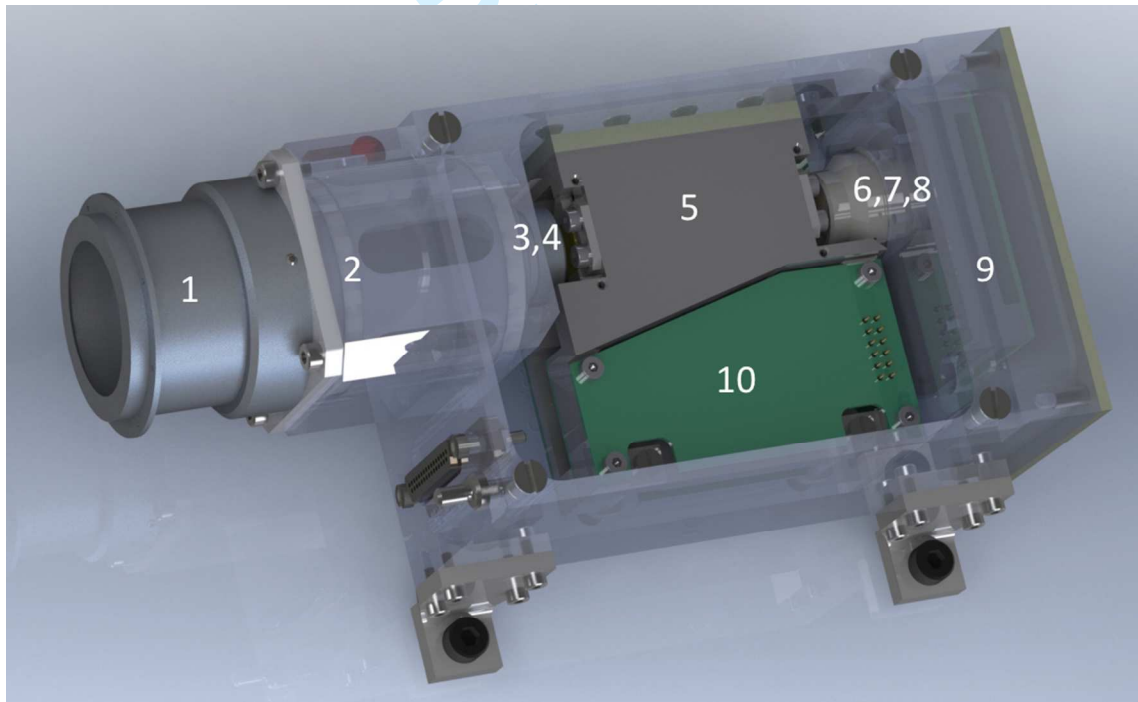


690

691

Figure 5. The block diagram of the ISEM control electronics.

692



693

694

695

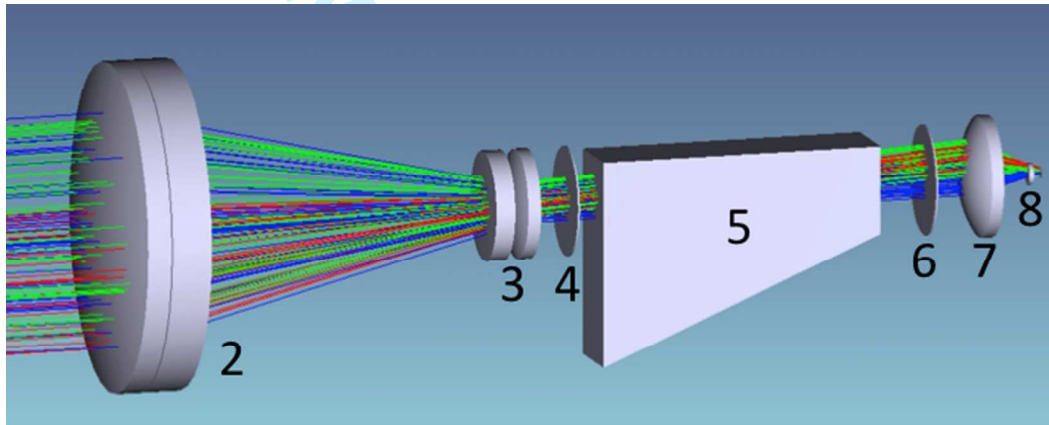
696

Figure 6. The 3D model open view of the ISEM Optical Box. The main elements are visible: 1- baffle, 2- entry optics; 3, 7- AOTF collimating optics; 4, 6- polarizers; 5- AOTF crystal; 8- detector; 9- detector's preamplifier; 10- AOTF RF

697 proximity electronics.

698

699 The spectrometer is built following a standard layout for an AOTF spectrometer,
700 with the AOTF in the path of a quasi-parallel beam. The optical scheme is based
701 on a Galileo system with remote pupil built using CaF_2 and ZnSe lenses and it is
702 presented in Fig. 7. The image is transferred through the optical system, and the
703 field-of-view (FOV) of 1.3° is formed on the detector sensitive area. The
704 achromatic lens entry telescope (1) has the aperture of 25 mm. The AOTF crystal
705 (5) is placed in a quasi-parallel beam between collimating lenses (3, 7), and a pair
706 of polarizers (4, 6); the output collimating lens (8) serves also as a focusing optic
707 for the detector (8).
708



709

710 Figure 7. ISEM optical scheme. The numbering is the same as in Fig. 6. 2-
711 foreoptics; 3, 7- AOTF collimating optics; 4, 6- polarizers; 5- AOTF crystal; 8-
712 sensitive area of the detector.

713

714 A wide-angle AOTF from NII Micropribor in Zelenograd, Russia is manufactured
715 on the base of a tellurium dioxide crystal. The ultrasound frequency range of 23-
716 82 MHz provides a spectral range from $1.15 \mu\text{m}$ to $3.3 \mu\text{m}$ with two
717 piezotransducers. The transducers operate in the sub-bands of 23-42 MHz and 42-
718 82 MHz. The crystal cut-off angle is 12.5° in the (110) crystallographic plane.
719 The anisotropic Bragg diffraction regime is used. The incident optical radiation
720 has ordinary polarization and the diffracted optical beam has the extraordinary
721 polarization. The angle between the passed and diffracted optical beams is 6° at
722 the output of the AO crystal. A pair of polarizers with crossed polarizing planes is
723 used to filter out the non-desired zero diffraction order.

1
2
3
4
5
6
7 724

8 725 The AOTF and its electronics are assembled in a single functional unit, which
9 726 includes the acousto-optic cell, the polarizers, a proximity RF matching board, an
10 727 RF synthesizer, the driver of the AO crystal (the RF power amplifier), and a
11 728 dedicated internal microcontroller, which communicates with the Main Controller
12 729 (MC) in the EB and controls all the functions of the acousto-optic module
13 730 (AOM). Commands define magnitude and frequency of the RF signal applied, as
14 731 well as the RF driver ON/OFF states. Within the RF range of 23-82 MHz, the
15 732 minimum step of frequency sweeping is 10 kHz (5900 frequency points). The RF
16 733 amplitude is may be set at one of 16 even levels. The AOM transmits back to the
17 734 MC a few housekeeping parameters, such as measured RF voltage, AO crystal
18 735 temperature, etc. The MC and the AOM are connected via an RS-485 interface
19 736 running at a speed of 115.2 Kbit/s.

20 737

21 738 During the measurement, the RF level is being alternated between ON and OFF
22 739 states, with the cadence being defined by integration time. The measured signal is
23 740 then processed as the AC allowing to remove offsets caused by the detector's dark
24 741 current and stray light, and improving the dynamic range of the instrument.

25 742

26 743 The detector is a single-pixel InAs thermo-electrically cooled photodiode. A
27 744 detector module J12TE3-66D-R01M from Teledyne Judson Technologies is used.
28 745 The built-in three-stage thermo-electric Peltier cooler maintains a detector
29 746 temperature about 90°C below that of the hot side. For the ISEM OB operating in
30 747 the range from -10° to +30°C, it results in the detector's temperature ranging
31 748 between -100° and -60°C, the corresponding detector's shunt resistance is
32 749 therefore 60-400 kOhms. The temperature of the sensitive area is monitored by a
33 750 built-in thermistor.

34 751

35 752 The detector's photocurrent is amplified with a two-stage circuit. The first stage is
36 753 a trans-impedance amplifier, AC-coupled (1 s time constant) to the second stage.
37 754 The second stage has a gain of 83 and a time constant of 80 μs and is based on an
38 755 ADA4610 (Analog Devices) operational amplifier characterized by low current
39 756 and voltage noise (50 fA Hz^{-1/2}, 7.5 nV Hz^{-1/2}). Its output signal is transmitted via
40 757 the harness to the Electronic Box.

41 758

42 759 **3.2 The Electronics Box**

1
2
3
4
5
6
7 760 The EB is mounted inside the rover at the rear balcony, and it is thermally
8 761 stabilized. It includes the ADC, the main and auxiliary controllers, power
9 762 conditioning (power supply unit, PSU), and the interface and bridge boards,
10 763 which support RS-422 communication between the ISEM and the Rover data and
11 764 command system.
12

13 765
14 766 The two ISEM blocks are connected via a 5-m harness running from the inside of
15 767 the Rover to the mast. It is fabricated by Thales Alenia Space-Italy (TAS-I). The
16 768 cable includes the analog signals from the detector and the thermal sensor, the
17 769 power supply lines and a digital RS-485 connection to control the AOFT RF
20 770 synthesizer and the power amplifier.
21

22 771
23 772 The Main Controller (MC) located in the EB commands the operation of all
24 773 modules of the instrument. It uses a MSP430FR5739 Texas Instruments circuit
25 774 running at 19.68 MHz. The controller is equipped with 1 Kbyte of RAM and 16
26 775 Kbyte of ferroelectric memory (FRAM) used for program and data storage.
27 776 Compared to commonly used FLASH memory, the FRAM has better radiation
28 777 immunity. A 10-bit internal ADC of the Main controller is used to digitize the
31 778 signal from the detector's thermistor.
32

33 779
34 780 The main ADC serves to digitize the signal from the detector, amplified in the OB.
35 781 A 16-bit ADC (ADS8320, Texas Instruments) is used. The full-scale range of the
36 782 ADC is 2.9 V and the peak-to-peak noise is 3 LSB (22 μ V RMS). The Main
37 783 Controller receives the ADC output data via a serial interface operating at 2
38 784 Mbit/s. The preamplifier and the ADC contribute little to the total noise in the
39 785 signal path, thus the Johnson noise of the detector controls the limit of signal
41 786 detection.
42

43 787
44 788 The Auxiliary controller, based on C8051F121 Silicon Laboratories circuit
45 789 operating at 12.25 MHz, incorporates a 12-bit ADC, and serves to monitor power
46 790 supply voltages and to dispatch the operation of different memory devices. In all,
47 791 ISEM employs two built-in FLASH memories within the microcontroller, and
48 792 two external chips of ferroelectric (FRAM) and magneto-resistive (MRAM)
49 793 memory.
50

51 794
52
53
54
55
56
57
58
59
60

1
2
3
4
5
6
7 795 The two microcontrollers hold four identical copies of their firmware in program
8 796 memories. At the start of operation, the controllers check the copies, repair
9 797 damaged ones and run a validation program. In order to increase its reliability,
10 798 ISEM contains two redundant main controller units. After turning on, first the
11 799 MC1 is powered. Its sequence, if performed correctly, commands the PSU to keep
12 800 power at MC1. If not commanded in 5 seconds, the PSU automatically powers on
13 801 the MC2, and so on.
14
15 802

16
17 803 The rover Onboard Computer (OBC) controls ISEM operations via RS-422
18 804 interface. There are two (nominal and redundant) RS-422 links. Communication
19 805 via only one of the links is available at a given time. The baud rate is 112.179
20 806 $\pm 1\%$ Kbit/s.
21
22 807

23 808 **3.3 The Calibration Target**

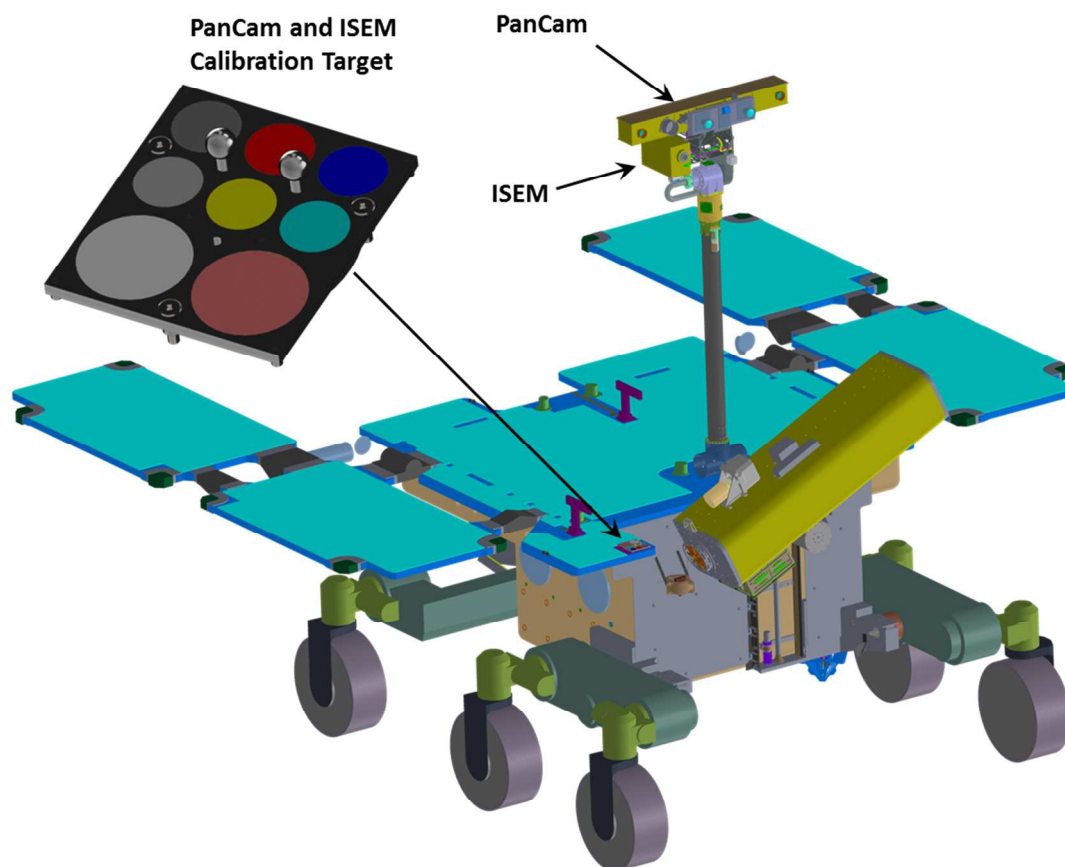
24
25 809 In order to determine the incident solar illumination spectrum for deriving I/F data,
26 810 and to verify the in-flight performance and stability of the instrument, ISEM will
27 811 observe the radiometric calibration target prior to each measurement. The target is
28 812 used for the in-flight radiometric calibration of both PanCam and ISEM, and will
29 813 be located on the front deck of the rover as shown in Fig. 8. At this location it will
30 814 be interrogated by ISEM from a distance of 1.1 m at an emittance angle of 24° .

31
32 815 The calibration target occupies an area of $67 \times 76 \text{ mm}^2$ and has a mass of 40 g.
33
34 816

35
36 817 The target includes 8 stained glass diffuse reflectance calibration patches with
37 818 different spectral reflectance properties. Two of these calibration patches will be
38 819 used by ISEM - the “white” which has a reflectance near 100% in the $0.4\text{-}3.0 \mu\text{m}$
39 820 spectral range, and the multiband patch, which has distinct spectral features. The
40 821 white patch is manufactured from Pyrocera provided by the Vavilov State
41 822 Optical Institute in St. Petersburg and the multiband patch is manufactured from
42 823 WCT-2065 — a rare earth doped glass manufactured by Schott and supplied by
43 824 Avian Technologies in the USA. The calibration patches will be calibrated for
44 825 absolute total hemispherical reflectance and Bidirectional Reflectance
45 826 Distribution Function (BRDF) and all measurement will be traceable to
46 827 photometric standards.
47
48 828

49
50 829 Dust deposition on the radiometric calibration target during the ExoMars mission
51 830 will be accounted for in the data processing by developing a model of the
52
53
54
55
56
57
58
59
60

1
2
3
4
5
6
7 831 calibration target and dust system, building on the results of previous missions,
8 832 measurements of settling rates on the rover panels, solar arrays, etc. (Kinch et al.
9 833 2007, 2015), and from PanCam calibration results.
10 834



40 835
41 836 Figure 8. PanCam and ISEM calibration target and its location on the rover.
42 837 Larger circles ($\text{\O}30$ mm) are for both ISEM and PanCam. The smaller circles
43 838 ($\text{\O}18$ mm) and the shadow posts will be used by PanCam only.
44
45

46 839

47 840

48 841 **4 Measurement Scenario**

49 842 **4.1 The Experiment Cycle**

50 843 The Experiment Cycle (EC) consists of one spectrum measurement by ISEM. It is
51 844 explained in Figure 9.

52 845
53
54
55
56
57
58
59
60

1
2
3
4
5
6
7 846 In order to eliminate the dark signal of the detector and any possible stray light
8 847 signal, the instrument measures photocurrents when the AOTF RF is OFF (the
9 848 dark signal) and when it is ON (the full signal). A subtraction of the two values
10 849 gives the true signal corresponding to the spectrally filtered radiation on the
11 850 detector.

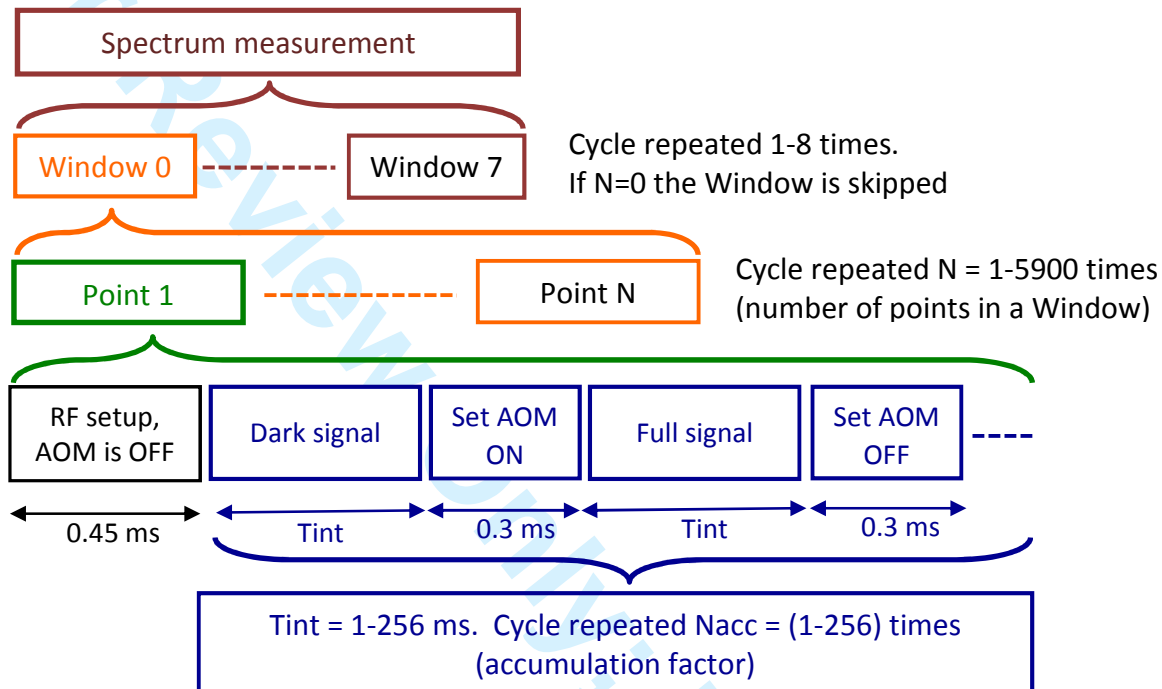
12 851
13
14 852 During both the ON and OFF states, the main ADC continuously samples signals
15 853 at a 20 kHz rate. The MC stacks all the measured values and makes the ON–OFF
16 854 subtraction. This elementary measurement can be repeated up to 256 times
17 855 (“accumulation factor” parameter), effectively increasing the integration time. All
18 856 resulting values are stacked as well. Each elementary measurement includes a
19 857 dead time of ~0.6 ms needed to turn the AOTF ON or OFF. These overheads are
20 858 mostly the result of remote commanding of the acousto-optic module in the OB,
21 859 but also include two 0.12-ms transients in the AOTF. An additional dead time of
22 860 0.45 ms is needed to change the RF. The integration time, variable between 1 and
23 861 256 ms and defining the ON/OFF timing, and the number of repeated ON/OFF
24 862 cycles for a given RF value (the accumulation factor) are set by a command.
25
26
27
28
29
30

31 863
32 864 As discussed above, the measurement time is a critical factor. To achieve
33 865 flexibility in spectral sampling, up to 8 “windows” can be defined for one
34 866 measurement of a spectrum. Every window can be placed anywhere in the AOM
35 867 frequency range and it has its own number of spectrum points, frequency steps,
36 868 and accumulation factors.
37
38

39 869
40 870 During an elementary measurement the 16-bit ADC readings add up to a 24-bit
41 871 value, and further accumulation, up to 256 times, results in a 32-bit value for each
42 872 spectrum point. Only 16 bits out of it are used, three options being (i) to transfer
43 873 merely the 16 LSBs, or (ii) 16 bits starting from a certain bit in order to remove
44 874 noise, or (iii) to normalize within one spectrum so that the maximum fits exactly
45 875 within 16 bits. In the latter case the risk is that an errant spike distorts the entire
46 876 spectrum.
47
48

49 877
50 878 The exchange of commands between ISEM and the OBC proceeds as follows.
51 879 The OBC transmits a command (TC) and Rover Elapsed Time (RET). The TC
52 880 defines ISEM operation parameters and triggers the spectrum measurement. The
53 881 RET command synchronizes ISEM’s internal time. In the course of operation, the
54
55
56
57
58
59
60

882 ISEM sends scientific and housekeeping packets to the OBC and these data are
 883 stored into the OBC memory.
 884



885

886

887 Figure 9. A diagram showing timing and breakdown of one spectrum
 888 measurement.

889

890 4.2 Operations on the surface

891

892 ISEM operations over the course of the Reference Surface Mission (RSM) are
 893 intimately connected those of the mast and PanCam. All operations are to be
 894 guided by the mast's pointing. Three basic operating regimes have been
 895 identified:

896

897 1) Operations to support sampling.

898 ISEM will work in parallel with PanCam, as shown in Fig. 2. First the WAC
 899 observes an area panoramically, and then the HRC is pointed to the most
 900 interesting spots. The spot must be illuminated by direct sunlight. At least one

1
2
3
4
5
6
7 901 ISEM spectrum is planned be acquired together with every HRC image, and
8 902 ISEM measurements may be also conducted separately. The ISEM data will be
9 903 used to characterize the mineral composition. Sometimes ISEM will be used
10 904 together with the WAC “geology” filters; however, full analysis with the PanCam
11 905 WAC geological filters is slower and produces much more data so this capability
12 906 cannot be used regularly.
13
14
15

16 907
17 908 2) Operations to assess the geology value of targets

18 909 A number of geologically interesting scenes may be distant from the planned
19 910 rover track or inaccessible for rover sampling, such as crater rims, outcrops, etc.
20 911 Remote characterization is the only possibility in this case. ISEM will be operated
21 912 in the same manner as in the first case. There is no theoretical limit on the
22 913 sounding range provided the illumination conditions (including the phase angle)
23 914 are acceptable. For instance, illuminated hill slopes may be observed from dozens
24 915 of km. A practical limit is determined by the ISEM’s FOV, a ~1-meter spot is
25 916 observed from 44-meter distance. This mode could be used for rover-orbiters
26 917 coordinated measurements and validations. For a favorable scene ISEM may
27 918 provide cross-validation over the area covering multiple CRISM pixels.
28
29
30
31

32 919
33 920 3) Dedicated environmental operations

34 921 ISEM data may be used to characterize atmospheric humidity and aerosol loading.
35 922 Some information will be obtained as a by-product of geological measurements
36 923 intermitted with observations of the calibration target. The information about the
37 924 gaseous atmospheric absorption will be assured by dense spectral sampling of the
38 925 appropriate spectral intervals. Aerosols are best characterized by cross sky
39 926 observations. PanCam WAC plans direct Sun observations and cross sky viewing
40 927 atmospheric campaigns. As discussed in Section 2.5, the ISEM capability to
41 928 observe the direct Sun is not confirmed. At the same time, following preliminary
42 929 laboratory characterization we do not expect any operational constraints placed by
43 930 ISEM on PanCam solar imaging.
44
45
46
47

48 931
49 932 In the case of cross sky imaging the ISEM line of sight will be oriented above the
50 933 horizon, and a special ISEM data acquisition sequence will be implemented. The
51 934 HRC measurements are not needed, and ISEM will observe in parallel with WAC.
52 935 The elevation and phase angle for these measurements needs to be carefully
53 936 planned, targeting as much as possible range of phase angles for WAC and
54
55
56
57
58
59
60

1
2
3
4
5
6
7 937 detectable scattered signal in the IR for ISEM.

8 938

9 **4.2 Resources required**

10 ISEM's data volume is relatively small. One spectrum is only two kilobytes in
11 size (see Table 1 and Section 3). The factor most affecting the rover operations is
12 the measurement time. Fixed surface platforms are better suited for lengthy
13 operations, generally allowing significant accumulation of measurements.
14 However, sequential acquisition of spectra effectively increases the recording
15 time, and, as a result, required measurement times become an important factor for
16 the rover operation cycle.
17
18
19

20 947

21 The allocated duration of measurements is from 2.5 min (minimum case) to 8.0
22 minutes (optimal case) for a single target. During the whole sequence, ISEM will
23 consume ~12W, requiring an energy of 0.5-4.4 Watts per hour. As described in
24 section 3.3 the length of the spectrum, or the number of points in the spectrum,
25 can be selected. For a "geology" target we will always measure across the full
26 spectral range of ISEM, which may be divided into 1-8 intervals with different
27 sampling. The total number of points in one spectrum will vary between 256 and
28 1024. Within the spectral range, some portions of the spectrum will be measured
29 more accurately, where e.g. a narrow mineral absorption feature or important
30 atmospheric absorption are expected, while other portions of smooth continuous
31 character can be undersampled.
32
33
34
35
36
37

38 959

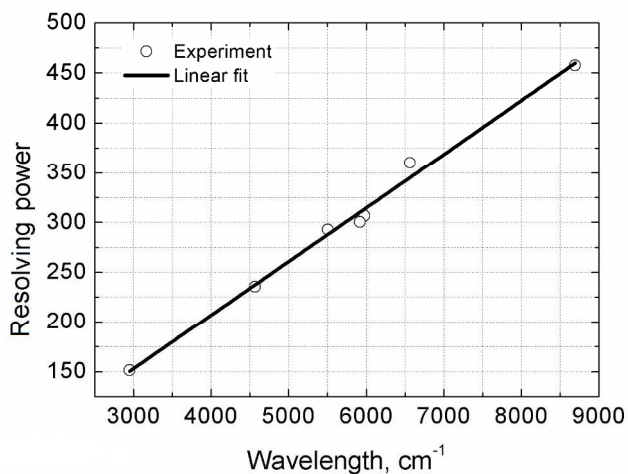
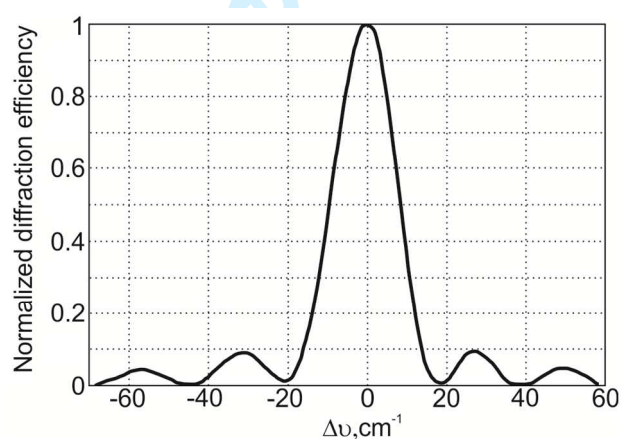
39 **4.3 Measurement performance, examples, comparison with state of the art**

40 As the full working prototype of ISEM has not been built yet, the performance of
41 the instrument was verified using the closest prototype, the qualification model
42 (QM) of LIS for the Luna 25 lander. The ISEM hardware involves some
43 improvements with respect to LIS, including better optical throughput (and more
44 sensitive detector featuring the three-stage Peltier cooler. The spectral properties
45 of the AOTF remain the same.
46
47

48 967

49 Spectral range and spectral resolution. The bounds of the spectral range were
50 verified using He-Ne 1.152 μm and 3.39 μm laser lines. The theoretical shape of
51 an AOTF spectral instrument function is close to sinc^2x . Side lobes of this
52 function modify the measured spectrum, but this could be readily accounted for
53 once the bandpass is properly characterized. More dangerous are distant side
54
55
56
57
58
59
60

lobes, which manifest themselves as a sort of stray light and may reduce the apparent depth of spectral features. More discussion on this aspect of AOTF characterization may be found in Korablev et al. (2013). The measured band pass transmission function of the ISEM prototype is shown in Fig. 10a. The evolution of the resolving power $\lambda/\Delta\lambda$ through the spectral range measured at multiple wavelengths using light sources with sharp emission features (different He-Ne laser, single-mode laser diodes, low-pressure gas-filled lamps) is shown in Fig. 10b.



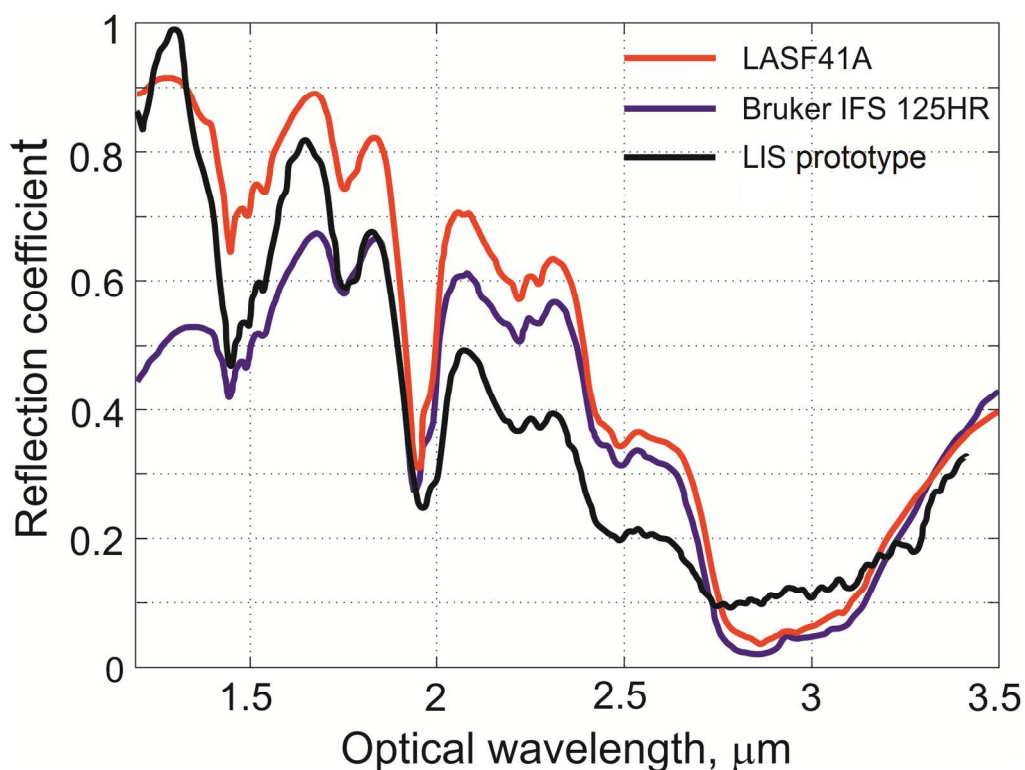
983

984

985 Figure 10. (a) Normalized transmission function of the instrument measured at
 986 1.523 μm laser line. The FWHM is 19 cm^{-1} (2.7 nm). (b) The resolving power
 987 measures through the full spectral range.

988

1
2
3
4
5
6
7 989 A simulation measurement of a mineral spectrum of a Mars analogue by LIS
8 990 prototype is presented in Fig. 11. Crystalline gypsum was manually ground and
9 991 sieved to obtain ~1-mm grains, and the resulting sample was illuminated with a
10 992 150-W halogen lamp from a distance of 18 cm. The full time to measure this
11 993 spectrum was 30 min, and the effective exposure to measure one spectral point
12 994 was 1 s in the long-wave AOTF sub-range, and 0.6 s in the short-wave sub-range.
13 995 The spectrum shown is normalized by a spectrum of a Lambertian screen (metal
14 996 surface covered by special reflective coating). The differences between the library
15 997 and measured spectra might be attributed to different origin of the samples; the
16 998 difference between the FTS and ISEM spectra are likely due to different
17 999 observation geometry.



46 1000
47 1001 Figure 11. A reflectance spectrum of crystalline gypsum measured by the closest
48 1002 equivalent of ISEM: LIS qualification prototype, and a laboratory Fourier-
49 1003 spectrometer (Bruker), compared to a CRISM library spectrum (LASF41A).
50 1004

51 1005 Signal-to-noise ratio estimation. The signal-to-noise ratio (S/N) of ISEM and its
52 1006 LIS prototype is limited by the detector background noise (see section 3.1), so we

1
2
3
4
5
6
7 1007 may estimate the S/N for ISEM based on LIS prototype testing. With 3 ms
8 1008 integration time repeated 6 times per point LIS provides the S/N~10 in the center
9 1009 of the spectral range and 3-5 on the edges. This estimation using the reflected
10 1010 sunlight and laboratory light sources involves many uncertainties, including
11 1011 transparency of the terrestrial atmosphere, scaling to the Sun intensity at Mars
12 1012 distance, and extrapolation. In turn there remains a margin on the duration of the
13 1013 measurement. The real time to measure one spectral point is not 18 ms, but
14 1014 $(3 \cdot 2 + 0.6) \cdot 6 + 0.45 = 40.05$ ms, because the light measurement is alternated with
15 1015 dark measurement, and there are some extra delays in the system (see section 4.1.)
16 1016 With 3 ms integration time the full spectrum is measured in 41 s, while the
17 1017 measurements at the surface of Mars may last 2.5-8 min (see section 4.2) that
18 1018 translates in sensitivity gain of 2-3.
19
20
21
22
23

24 1020 The improvements in ISEM with respect to LIS are i) the deeply cooled detector
25 1021 with a peak sensitivity attaining a factor of 10 better, and ii) the larger throughput
26 1022 of the entry optics and the AOTF: The LIS f-number is F:6; the improved ISEM
27 1023 throughput is ~F:1.7, but vignetting in the AOTF results in effective throughput of
28 1024 ~F:2. The resulting gain factor is therefore ~90. The detector's peak sensitivity is
29 1025 at 3.3 μm in both cases but the curve for the LIS detector is somewhat more flat.
30 1026 The AOTF characteristics may vary as well. Using more conservative factor of 30
31 1027 the resulting S/N of ISEM can be estimated as ~300 in the center of the range, and
32 1028 100-150 at the edges.
33
34
35
36
37

38 1030 Estimation of detection capabilities. Starting from the S/N estimation above we
39 1031 may estimate minimum detectable abundance for minerals discussed in section
40 1032 2.4 (see Fig. 1). Precaution factors in the measurement time (2-3), and in
41 1033 sensitivity (~3) allow sufficient margin to account for, e.g, unfavorable phase
42 1034 angle, or other factors. We used spectra of different minerals of interest (Fig. 1 a-
43 1035 f) , on the background spectra of "bright" and "dark" regions of Mars (Erard
44 1036 1997) to simulate the reflectance of an admixture to the bulk spectrum of the
45 1037 martian surface. The preliminary sensitivity estimates to detect the fraction of the
46 1038 selected mineral are presented in Table 3. Given relatively high ISEM S/N ratio
47 1039 deduced above, these estimates based on the relative depth of individual spectral
48 1040 features are very conservative. A better sensitivity analysis is planned in the
49 1041 future, involving analysis of martian mineral analogues, and multicomponent
50 1042 analysis.
51
52
53
54
55
56
57
58
59
60

1043

1044 Table. 3. Preliminary estimation of the ISEM sensitivity to detect different
 1045 minerals and mineral groups from CRISM spectral library (Fig. 1) on the
 1046 background of bright and dark region Mars spectra (Erard, 1997). Mineral
 1047 features used to estimate the sensitivity are listed in the last column.

Mineral or mineral group	Bright region	Dark region	Comment
Kaolinite (Fig. 1a)	<5%	5-10%	1.4, 2.2, 2.4 μm
Montmorillonite (Fig. 1b)	5-10%	10-15%	1.4, 1.9, 2.2-2.3 μm
Serpentine (Fig. 1c)	5-10%	5-10%	1.4, 2, 2.35 μm
Carbonates (Fig. 1d)	5-10%	~10%	2.3, 2.5, 3.4 μm
Gypsum (Fig. 1e)	~5%	5-10%	1.4-1.6, 1.8, 2.2 μm
Kieserite (Fig. 1e)	<5%	~10%	Broad structure 1.4-2.4 μm
Jarosite (Fig. 1f)	<5%	5-10%	1.48, 1.75, 2.25 etc. μm

1048

1049 The issue of detection capabilities can be divided into two broad categories: (1)
 1050 characterization of a target in the presence of windblown dust; and (2) detection
 1051 of a phase or phases of interest in a multicomponent assemblages. There are a
 1052 number of studies that have examined detection limits for various components
 1053 that are relevant to this issue, and these are supplemented by ongoing studies by
 1054 our team that are designed to specifically address this issue. The results of these
 1055 studies are summarized in Table 4 below. Some selected examples are shown in
 1056 Figures 12-14.

1057

1058 Detection limits depend on a wide variety of factors, beside end member
 1059 abundances. These include factors such as relative grain size, the availability of
 1060 diagnostic absorption bands, the relative intensity of diagnostic absorption bands,
 1061 and physical properties such as whether phases of interest are physically mixed,
 1062 or whether an obscuring phase, such as dust cover is present.

1063

1064 We have found that, at least for the variety of mixtures examined, detection limits
 1065 are on the order of 10-25 wt.%. For some phases, such as certain organic
 1066 compounds, detection limits are much lower (e.g, 1 wt.% adenine is detectable in
 1067 the presence of 99 wt.% nontronite (an iron-bearing clay) or hematite (an iron
 1068 oxide) (Figures 13 and 14)). Further extensive tests of mineral mixtures and

1069 detection limits are ongoing and planned.

1070

1071 Table 4. Summary of some studies concerning detection limits and discrimination

1072 of different phases relevant to the capabilities of ISEM

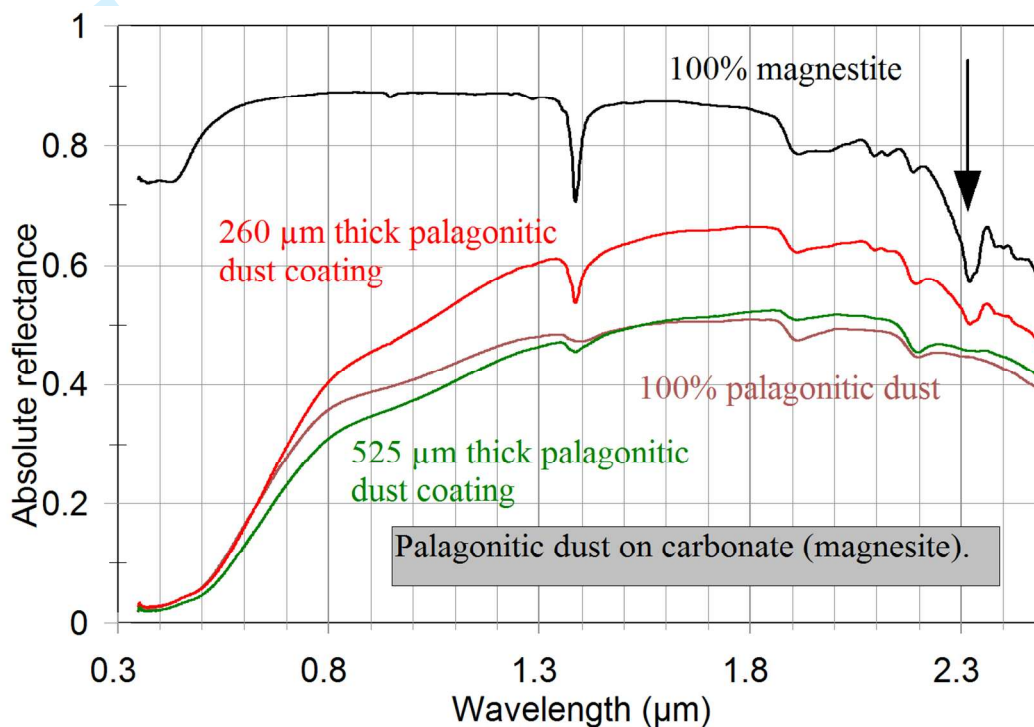
Mixture type	Detection limit	Characteristic spectral features	Source
Orthopyroxene + clinopyroxene	~15% of either phase	2 μm region	Cloutis and Gaffey (1991)
Olivine + orthopyroxene	~20% olivine, 5% pyroxene	2 μm region	Cloutis et al. (1986)
Orthopyroxene + clinopyroxene	~15% of either phase	2 μm region	Cloutis and Gaffey (1991)
Pyroxene + palagonitic dust (spectral equivalent of Mars dust) or hematite	~10% pyroxene	2 μm region	Cloutis and Bell (2004)
Carbonate + basalt	~20% carbonate	2.3-2.6 μm region	Palomba et al. (2009) and this study
Carbonate + palagonitic dust (Fig. 12)	~15% carbonate	2.3-2.6 μm region	Palomba et al. (2009) and this study
Palagonitic dust on carbonate (Fig. 12)	<~500 μm thick palagonite coating required	2.3, 2.5 μm regions	This study
Palagonitic dust on basalt	<~250 μm thick palagonite coating required		This study
Kaolinite + illite	~20% of either phase	2.2-2.5 μm region	This study
Gypsum + basalt	~5% gypsum	1.4, 1.9 μm regions	This study
Gypsum + palagonitic dust	~5% gypsum	1.4, 1.9 μm regions	This study
Pyroxene + volcanic glass	~15% pyroxene	2 μm region	This study
Palagonitic dust + carbonate	~20% carbonate	2.3, 2.5 μm regions	This study
Nontronite + adenine (Fig. 13)	~1% adenine	1.65, 2.2 μm regions	This study
Hematite + adenine	~1% adenine	1.65, 2.2 μm	This study

(Fig. 14)		regions	
-----------	--	---------	--

1073

1074

1075



1076

1077

1078

1079

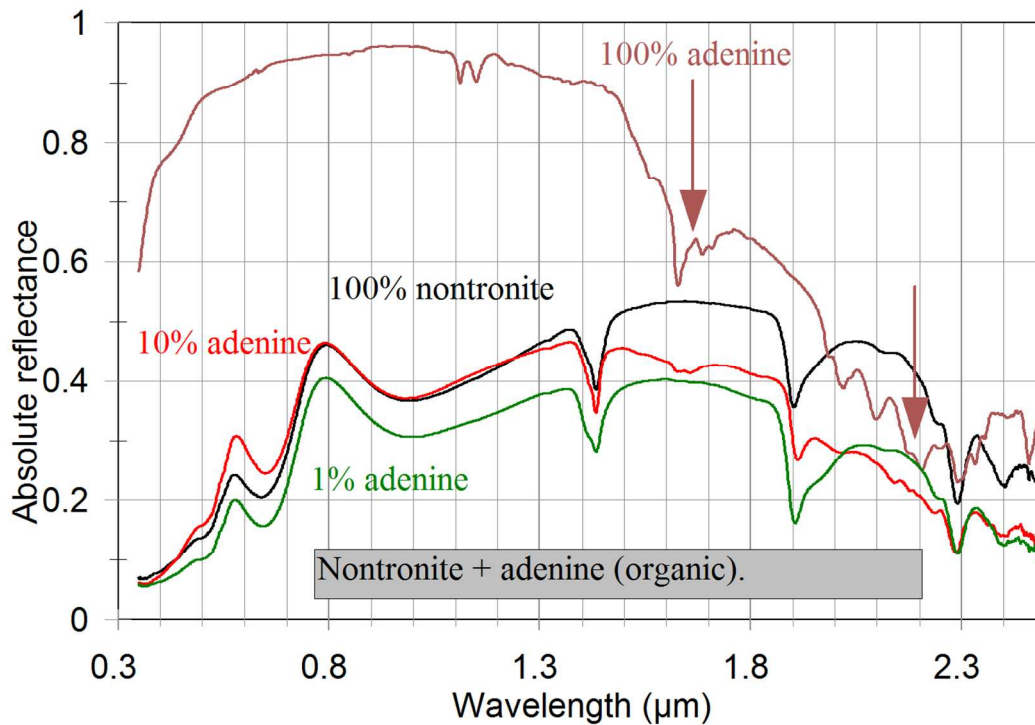
1080

1081

1082

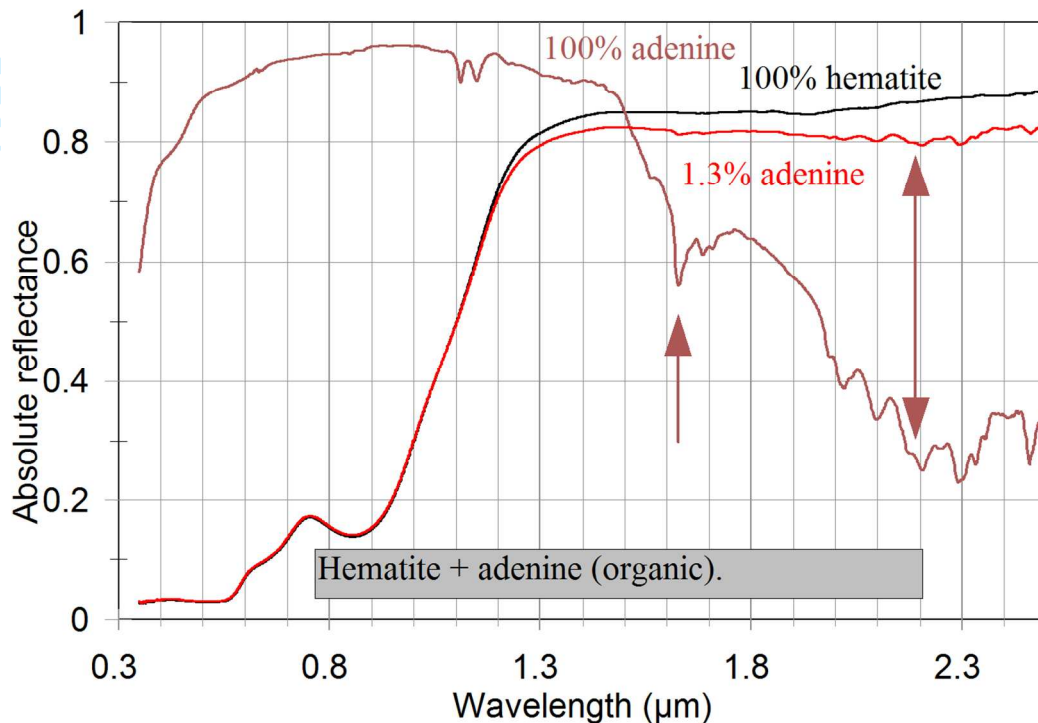
1083

Figure 12. Reflectance spectra of palagonitic dust sprinkled on a powdered carbonate (magnesite). The most diagnostic absorption band, near 2.33 μm is indicated by an arrow. Note that the band is clearly present with a 260 μm palagonitic dust coating. It is still present, but barely discernible for a 525 μm thick dust coating.



1084
1085
1086
1087
1088
1089

Figure 13. Reflectance spectra of intimate mixtures of nontronite (an Fe-rich clay) and adenine (a component of DNA). The brown arrows indicate spectral regions where adenine absorption bands are still detectable when only 1 wt.% of adenine is present in the mixtures.



1090

1091 **Figure 14.** Reflectance spectra of intimate mixtures of hematite (an Fe-oxide) and
1092 adenine (a component of DNA). The brown arrows indicate spectral regions
1093 where adenine absorption bands are still detectable when only 1.3 wt.% of
1094 adenine is present in the mixtures.

1095

1096

1097 **4.4. Environmental requirements and characterization**

1098 The placement of the ISEM optical head on the Rover mast with no possibility of
1099 thermal control imposes stringent requirements on survival temperature. The
1100 AOTF is a critical device involving bonding of highly anisotropic materials, such
1101 as TeO_2 and LiNbO_3 . Anisotropic thermal expansion makes the AOTF devices
1102 vulnerable to large temperature excursion, in particular at low temperatures.
1103 AOTF technology has demonstrated survival and even operation down to -130°C
1104 and below (Leroi et al, 2009; Mantsevich et al, 2015). Several non-operational
1105 thermal cycles attaining -130°C lower bound were also performed on two
1106 dedicated ISEM acousto-optic components; more testing to fully validate the
1107 technology is to be completed.

1108

1
2
3
4
5
6
7 1109 An important aspect of the AOTF spectrometer characterization is the thermal
8 1110 calibration, because the optical heads are intended for operations across a
9 1111 relatively wide temperature range. Some results of thermal characterization of the
10 1112 acousto-optic module are described in Mantsevich et al. (2015). The operation of
11 1113 the AO filters was tested in the range of -50° to $+40^{\circ}\text{C}$. The temperature affects
12 1114 the elastic properties of TeO_2 , changing the ultrasound velocity and birefringence.
13 1115 The variation of the TeO_2 refraction coefficient as a function of temperature is
14 1116 negligible. In turn, the change of the slow acoustic wave velocity causes a
15 1117 noticeable shift of the dispersion curve, comparable with the AO filter pass band
16 1118 in the operating temperature range. The characterization of the flight instrument
17 1119 will therefore include calibration of the dispersion curve within the operational
18 1120 temperature range.
19 1121

1122 **5. Conclusions**

1123 Sampling from beneath the martian surface to reach and to analyze material
1124 unaltered or minimally affected by cosmic radiation is a significant feature and
1125 perhaps the strongest advantage of the ExoMars rover. The selection of the
1126 sampling sites and, in more general terms, the remote reconnaissance and studies
1127 of the landing site area, are a major part of the Rover's mission. ISEM offers a
1128 method of mineralogical characterization using IR reflectance spectroscopy, a
1129 technique well proven in orbital studies, and expected to be even more valuable
1130 and precise at the local scale.
1131

1132 In the coming year we aim to deliver field-compatible hardware and to participate
1133 in tests at terrestrial analogue sites and in other joint validations of instrument
1134 performance with the ExoMars team.
1135

1136 **Acknowledgements**

1137 ExoMars is a joint space mission of European Space Agency and Roscosmos.
1138 ISEM development is funded by Roscosmos under direct contracts to IKI, NE,
1139 AAF, and AYT acknowledge support from Russian Science Foundation (grant
1140 number RSF 16-12-10453), which enabled assessment of measurement
1141 characteristics of the instrument and the associated modeling. We are grateful to
1142 P.N. Lebedev Physical Institute of the Russian Academy of Sciences for the use
1143 of Bruker Fourier spectrometer facility. EAC thanks the Canadian Space Agency,
1144 the Canada Foundation for Innovation, the Manitoba Research Innovation Fund,

1
2
3
4
5
6
7 1145 the Natural Sciences and Engineering Research Council of Canada, and the
8 1146 University of Winnipeg for supporting the establishment and operation of the
9 1147 Planetary Spectrophotometer Facility at the University of Winnipeg.
10 1148 Development and manufacture of the calibration target is carried out in
11 1149 collaboration with the PanCam instrument team and funded by the UK Space
12 1150 Agency, grant numbers ST/L001454/1, ST/N003349/1 and ST/N006410/1. We
13 1151 thank Dr. Helen Miles for rendering the graphic in Fig. 1. We thank Manish Patel
14 1152 and an anonymous reviewer, whose comment helped to improve this paper. We
15 1153 also express our sincere gratitude to the space agencies, countries, companies, and
16 1154 project teams working to make the ExoMars mission possible.
17
18
19
20

21 1155
22 1156 ISEM Science team: Korablev O.I, Altieri F, Basilevsky A.T, Belyaev, D, Bibring
23 1157 J.P, Carter, J, Cloutis E, Demidov N, Esposito F, Evdokimova N.A, Fedorova
24 1158 A.A, Flahaut J, Gerasimov M.V, Griffiths A, Gunn M, Karatekin O, Kilian R,
25 1159 Kuzmin R.O, Mantsevich S.N, Martín-Torres J, Poulet F, Rodionov D.S, Schmitz
26 1160 N, Vago J, Zorzano M.-P.
27
28

29 1161
30 1162 ISEM Technical team: Dobrolensky Yu, Alexandrov, K, Arefyev V,
31 1163 Brekhovskikh Yu.A, Buntov M.V, Dzuiban, I, Ivanov Yu.S, Kalinnikov Yu. K,
32 1164 Kozlova T.O, Kozlov O.E, Makarenko V, Martynovich F, Muratov A, Patrakeev
33 1165 A.S, Rotova N.V, Sapgir A.G, Semena N, Smirnova, A, Stepanov A.V, Titov
34 1166 A.Yu, Trokhimovskiy A.Yu, Vyazovetsky N.A.
35
36
37
38

39 1169 **References**

40 1170
41 1171 Allwood AC, Burch IW, Rouchy JM, and Coleman M. (2013) Morphological
42 1172 Biosignatures in Gypsum: Diverse Formation Processes of Messinian (~6.0
43 1173 Ma) Gypsum Stromatolites. *Astrobiology*, 13, 870-886.
44 1174 Anders E, Shearer CK, Papike JJ, Bell JF, Clemett SJ, Zare RN, McKay DS,
45 1175 Thomas-Keprta KL, Romanek CS, Gibson EK, Jr. and others. (1996)
46 1176 Evaluating the Evidence for Past Life on Mars. *Science*, 274, 2119-2125.
47 1177 Applin DM, Izawa MRM, Cloutis EA, Goltz D, and Johnson JR. (2015) Oxalate
48 1178 minerals on Mars? *Earth Planet Sci Lett*, 420, 127-139.
49
50
51
52
53
54
55
56
57
58
59
60

- 1
2
3
4
5
6
7 1179 Applin DM, Izawa MRM, and Cloutis EA. (2016) Reflectance spectroscopy of
8 1180 oxalate minerals and relevance to Solar System carbon inventories. *Icarus*,
9 1181 278, 7-30.
- 10 1182 Bandfield JL, Amador ES, and Thomas NH. (2013) Extensive hydrated silica
11 1183 materials in western Hellas Basin, Mars. *Icarus*, 226, 1489-1498.
- 12 1184 Bandfield JL, Hamilton VE, and Christensen PR. (2000) A Global View of
13 1185 Martian Surface Compositions from MGS-TES. *Science*, 287, 1626-1630.
- 14 1186 Bandfield JL, Hamilton VE, Christensen PR, and McSween HY. (2004)
15 1187 Identification of quartzofeldspathic materials on Mars. *J Geophys Res*, 109,
16 1188 E10009.
- 17 1189 Beck P, Quirico E, Sevestre D, Montes-Hernandez G, Pommerol A, and Schmitt
18 1190 B. (2011) Goethite as an alternative origin of the 3.1 μm band on dark
19 1191 asteroids. *Astron Astrophys*, 526, A85-A88.
- 20 1192 Berg BL, Cloutis EA, Beck P, Vernazza P, Bishop JL, Takir D, Reddy V, Applin
21 1193 D, and Mann P. (2016) Reflectance spectroscopy (0.35-8 μm) of ammonium-
22 1194 bearing minerals and qualitative comparison to Ceres-like asteroids. *Icarus*,
23 1195 265, 218-237.
- 24 1196 Bibring JP, Combes M, Langevin Y, Gara C, Drossart P, Encrenaz T, Frard S,
25 1197 Forni O, Gondet B, Ksanfomality L, and others. (1990) First results of the
26 1198 ISM experiment. *Pisma v Astronomicheskii Zhurnal*, 16, 318-322.
- 27 1199 Bibring J-P, Soufflot A, Berthé M, Langevin Y, Gondet B, Drossart P, Bouyé M,
28 1200 Combes M, Puget P, Semery A and others. (2004) OMEGA: Observatoire
29 1201 pour la Minéralogie, l'Eau, les Glaces et l'Activité. In: *Mars Express: the*
30 1202 *Scientific Payload*. Ed. Wilsons A, ESA Publications Division, ESA SP-1240,
31 1203 p 37-49.
- 32 1204 Bibring JP, Langevin Y, Mustard JF, Poulet F, Arvidson R, Gendrin A, Gondet B,
33 1205 Mangold N, Pinet P, Forget F and others. (2006) Global Mineralogical and
34 1206 Aqueous Mars History Derived from OMEGA/Mars Express Data. *Science*,
35 1207 312, 400-404.
- 36 1208 Bibring J-P, Hamm V, Pilorget C. (2017) The MicrOmega investigation onboard
37 1209 ExoMars. *Astrobiology*, this issue.
- 38 1210 Bishop JL, Loizeau D, McKeown NK, Saper L, Dyar MD, Des Marais DJ,
39 1211 Parente M, and Murchie SL. (2013) What the ancient phyllosilicates at
40 1212 Mawrth Vallis can tell us about possible habitability on early Mars. *Planet*
41 1213 *Space Sci*, 86, 130-149.
- 42
43
44
45
46
47
48
49
50
51
52
53
54
55
56
57
58
59
60

- 1
2
3
4
5
6
7 1214 Bishop JL, Quinn R, and Dyar MD. (2014) Spectral and thermal properties of
8 1215 perchlorate salts and implications for Mars. *American Mineralogist*, 99,
9 1216 1580-1592.
- 10 1217 Blake DF, Morris RV, Kocurek G, Morrison SM, Downs RT, Bish D, Ming DW,
11 1218 Edgett KS, Rubin D, Goetz W, and others. (2013) Curiosity at Gale Crater,
12 1219 Mars: Characterization and Analysis of the Rocknest Sand Shadow. *Science*,
13 1220 341, 5.
- 14 1221 Boyd SR (2001) Ammonium as a biomarker in Precambrian metasediments.
15 1222 *Precambrian Research*, 108, 159-173.
- 16 1223 Carrozzo FG, Bellucci G, Altieri F, D'Aversa E, and Bibring JP. (2009) Mapping
17 1224 of water frost and ice at low latitudes on Mars. *Icarus*, 203, 406-420.
- 18 1225 Carter J, and Poulet F. (2013) Ancient plutonic processes on Mars inferred from
19 1226 the detection of possible anorthositic terrains. *Nature Geosci*, 6, 1008-1012.
- 20 1227 Carter J, Poulet F, Bibring JP, Mangold N, and Murchie S. (2013) Hydrous
21 1228 minerals on Mars as seen by the CRISM and OMEGA imaging
22 1229 spectrometers: Updated global view. *J Geophys Res*, 118, 831-858.
- 23 1230 Christensen PR, Bandfield JL, Smith MD, Hamilton VE, and Clark RN. (2000)
24 1231 Identification of a basaltic component on the martian surface from Thermal
25 1232 Emission Spectrometer data. *J Geophys Res*, 105, 9609-9621.
- 26 1233 Christensen PR, Bandfield JL, Hamilton VE, Ruff SW, Kieffer HH, Titus TN,
27 1234 Malin MC, Morris RV, Lane MD, Clark RL, and Jakosky BM. (2001) Mars
28 1235 Global Surveyor Thermal Emission Spectrometer experiment: investigation
29 1236 description and surface science results. *J Geophys Res*, 106, 23823-23871.
- 30 1237 Christensen PR, Mehall GL, Silverman SH, Anwar S, Cannon G, Gorelick N,
31 1238 Kheen R, Tourville T, Bates D, Ferry S, and Fortuna T. (2003) Miniature
32 1239 thermal emission spectrometer for the Mars Exploration rovers. *J Geophys*
33 1240 *Res*, 108, 8064.
- 34 1241 Christensen PR, Ruff SW, Ferguson RL, Knudson AT, Anwar S, Arvidson RE,
35 1242 Bandfield JL, Blaney DL, Budney C, Calvin WM, and others. (2004) Initial
36 1243 Results from the Mini-TES Experiment in Gusev Crater from the Spirit
37 1244 Rover. *Science*, 305, 837-842.
- 38 1245 Christensen PR, Wyatt MB, Glotch TD, Rogers AD, Anwar S, Arvidson RE,
39 1246 Bandfield JL, Blaney D.L, Budney C, Calvin WM, and Fallacaro A. (2004)
40 1247 Mineralogy at Meridiani Planum from the Mini-TES experiment on the
41 1248 Opportunity Rover. *Science*, 306, 1733-1739.
- 42
43
44
45
46
47
48
49
50
51
52
53
54
55
56
57
58
59
60

- 1
2
3
4
5
6
7 1249 Clark RN, King TVV, Klejwa M, Swayze GA, and Vergo N. (1990) High spectral
8 1250 resolution reflectance spectroscopy of minerals. *J Geophys Res*, 95, 12653-
9 1251 12680.
- 10 1252 Clark RN, Curchin JM, Hoefen TM, and Swayze GA. (2009) Reflectance
11 1253 spectroscopy of organic compounds: 1. Alkanes. *J Geophys Res*, 114, 1-19.
- 12 1254 Cloutis EA, and Bell III JF. (2004) Mafic silicate mapping on Mars: Effects of
13 1255 palagonitic material, multiple mafic silicates, and spectral resolution. *Icarus*,
14 1256 172, 233-254.
- 15 1257 Cloutis EA, and Gaffey MJ. (1991) Pyroxene spectroscopy revisited: Spectral-
16 1258 compositional correlations and relationship to geothermometry. *J Geophys*
17 1259 *Res*, 96, 22809-22826.
- 18 1260 Cloutis EA, and Gaffey MJ. (1991) Spectral-compositional variations in the
19 1261 constituent minerals of mafic and ultramafic assemblages and remote sensing
20 1262 implications. *Earth, Moon, Planets*, 53, 11-53.
- 21 1263 Cloutis EA, Gaffey MJ, Jackowski TL, and Reed KL. (1986) Calibrations of
22 1264 phase abundance, composition, and particle size distribution for olivine-
23 1265 orthopyroxene mixtures from reflectance spectra. *J Geophys Res*, 91, 11641-
24 1266 11653.
- 25 1267 Cloutis EA, Hawthorne FC, Mertzman SA, Krenn K, Craig MA, Marcino D,
26 1268 Methot M, Strong J, Mustard JF, Blaney DL, Bell III JF, and Vilas F. (2006)
27 1269 Detection and discrimination of sulfate minerals using reflectance
28 1270 spectroscopy. *Icarus*, 184, 121-157.
- 29 1271 Cloutis EA, Craig MA, Mustard JF, Kruzelecky RV, Jamroz WR, Scott A, Bish
30 1272 DL, Poulet F, Bibring JP, and King PL. (2007) Stability of hydrated minerals
31 1273 on Mars. *Geophys Res Lett*, 34, L20202.
- 32 1274 Cloutis EA, Craig MA, Kruzelecky RV, Jamroz WR, Scott A, Hawthorne FC, and
33 1275 Mertzman SA. (2008) Spectral reflectance properties of minerals exposed to
34 1276 simulated Mars surface conditions. *Icarus*, 195, 140-168.
- 35 1277 Cloutis EA, Berg B, Mann P, and Applin D. (2016) Reflectance spectroscopy of
36 1278 low atomic weight and Na-rich minerals: Borates, hydroxides, nitrates,
37 1279 nitrites, and peroxides. *Icarus*, 264, 20-36.
- 38 1280 Coates AJ, and others (2017) ExoMars PanCam. *Astrobiology* this issue.
- 39 1281 Cull SC, Arvidson RE, Catalano JG, Ming DW, Morris RV, Mellon MT, and
40 1282 Lemmon M. (2010) Concentrated perchlorate at the Mars Phoenix landing
41 1283 site: Evidence for thin film liquid water on Mars. *Geophys Res Lett*, 37,
42 1284 L22203.
- 43
44
45
46
47
48
49
50
51
52
53
54
55
56
57
58
59
60

- 1
2
3
4
5
6
7 1285 Ehlmann BL, Mustard JF, Murchie SL, Poulet F, Bishop JL, Brown AJ, Calvin,
8 1286 WM, Clark RN, Marais DJD, Milliken RE, and others. (2008) Orbital
9 1287 identification of carbonate-bearing rocks on Mars. *Science*, 322, 1828-1832.
10 1288 Ehlmann BL, Mustard JF, Swayze GA, Clark RN, Bishop JL, Poulet F, Des
11 1289 Marais DJ, Roach LH, Milliken RE, Wray JJ and others. (2009) Identification
12 1290 of hydrated silicate minerals on Mars using MRO-CRISM: Geologic context
13 1291 near Nili Fossae and implications for aqueous alteration. *J Geophys Res*, 114,
14 1292 E00D08.
15
16
17 1293 Ehlmann BL, Mustard JF, and Murchie SL. (2010) Geologic setting of serpentine
18 1294 deposits on Mars. *Geophys Res Lett*, 37, 6201.
19
20 1295 Erard S. (2001) A spectro-photometric model of Mars in the near-infrared.
21 1296 *Geophys Res Lett*, 28, 1291-1294.
22
23 1297 Farley KA, Martin P, Archer PD Jr., Atreya SK, Conrad PG, Eigenbrode JL,
24 1298 Fairén AG, Franz HB, Freissinet C, Glavin DP, and others. (2016) Light and
25 1299 variable $^{37}\text{Cl}/^{35}\text{Cl}$ ratios in rocks from Gale Crater, Mars: Possible signature
26 1300 of perchlorate. *Earth Planet Sci Lett*, 438, 14-24.
27
28 1301 Fedorova AA, Montmessin F, Rodin AV, Korablev OI, Määttänen A, Maltagliati
29 1302 L, and Bertaux JL. (2014) Evidence for a bimodal size distribution for the
30 1303 suspended aerosol particles on Mars. *Icarus*, 231, 239-260.
31
32 1304 Flahaut J, Massé M, Le Deit L, Thollot P, Bibring JP, Poulet F, Quantin C,
33 1305 Mangold N, Michalski J, and Bishop JL. (2014) Sulfate-rich deposits on
34 1306 Mars: A review of their occurrences and geochemical implications. *LPI*
35 1307 *Contribution*, 1791, 1196.
36
37 1308 Forget F, Spiga A, Dolla B, Vinatier S, Melchiorri R, Drossart P, Gendrin A,
38 1309 Bibring J-P, Langevin Y, and Gondet B. (2007) Remote sensing of surface
39 1310 pressure on Mars with the Mars Express/OMEGA spectrometer: 1. Retrieval
40 1311 method. *J Geophys Res Planets*, 112, E08S15.
41
42 1312 Fouchet T, Montmessin F, Forni O, Maurice S, Wiens RC, Johnson JR, Clegg SM,
43 1313 Beck P, Poulet F, Gasnault O, et al. (2015) The infrared investigation on the
44 1314 SuperCam instrument for the Mars2020 rover. *LPI Contribution*, 1832, 1736.
45
46 1315 Freissinet C, Glavin, DP, Mahaffy PR, Miller KE, Eigenbrode JL, Summons RE,
47 1316 Brunner AE, Buch A, Szopa C, Archer PD, and others. (2015) Organic
48 1317 molecules in the Sheepbed Mudstone, Gale Crater, Mars. *J Geophys Res*, 120,
49 1318 495-514.
50
51 1319 Gendrin A, Mangold N, Bibring JP, Langevin Y, Gondet B, Poulet F, Bonello G,
52 1320 Quantin C, Mustard J, Arvidson R, and others. (2005) Sulfates in martian
53
54
55
56
57
58
59
60

- 1
2
3
4
5
6
7 1321 Layered Terrains: The OMEGA/Mars Express View. *Science*, 307, 1587-
8 1322 1591.
- 9 1323 Grotzinger JP, Sumner DY, Kah LC, Stack K, Gupta S, Edgar L, Rubin D, Lewis
10 1324 K, Schieber J, Mangold N and others. (2014) A habitable fluvio-lacustrine
11 1325 environment at Yellowknife Bay, Gale crater, Mars. *Science*, 343, 386.
- 12 1326 Hanley J, Chevrier VF, Barrows RS, Swaffer C, and Altheide TS. (2015) Near-
13 1327 and mid-infrared reflectance spectra of hydrated oxychlorine salts with
14 1328 implications for Mars. *J Geophys Res*, 120, 1415-1426.
- 15 1329 Hanley J, Chevrier VF, Dalton JB, and Jamieson CS. (2011) Reflectance spectra
16 1330 of low-temperature chloride and perchlorate hydrates relevant to planetary
17 1331 remote sensing. *LPI Contribution*, 1608, 2327.
- 18 1332 He ZP, Wang BY, Lu G, Li CL, Yuan LY, Xu R, Chen K, and Wang JY. (2014)
19 1333 Visible and near-infrared imaging spectrometer and its preliminary results
20 1334 from the Chang'E 3 project. *Rev Sci Instrum*, 85, 083104.
- 21 1335 Hecht MH, Kounaves SP, Quinn RC, West SJ, Young SMM, Ming DW, Catling
22 1336 DC, Clark BC, Boynton WV, Hoffman J, and others. (2009) Detection of
23 1337 perchlorate and the soluble chemistry of martian soil at the Phoenix Lander
24 1338 site. *Science*, 325, 64-67.
- 25 1339 Hunt GR, and Salisbury JW. (1970) Visible and near infrared spectra of minerals
26 1340 and rocks. *Modern Geol*, 1, 283-300.
- 27 1341 Izawa MRM, Applin DM, Norman L, and Cloutis EA. (2014) Reflectance
28 1342 spectroscopy (350-2500 nm) of solid-state polycyclic aromatic hydrocarbons
29 1343 (PAHs). *Icarus*, 237, 159-181.
- 30 1344 Kinch KM, Sohl-Dickstein J, Bell JF, Johnson JR, Goetz W and Landis GA.
31 1345 (2007). Dust deposition on the Mars Exploration Rover Panoramic Camera
32 1346 (Pancam) calibration targets. *J Geophys Res*, 112, E06S03.
- 33 1347 Kinch KM, Bell JF, Goetz W, Johnson JR, Joseph J, Madsen MB and Sohl-
34 1348 Dickstein J. (2015). Dust deposition on the decks of the Mars Exploration
35 1349 Rovers: 10 years of dust dynamics on the Panoramic Camera calibration
36 1350 targets. *Earth Space Science*, 2, 144–172.
- 37 1351 Korablev O, Bertaux JL, Fedorova A, Fonteyn D, Stepanov A, Kalinnikov Y,
38 1352 Kiselev A, Grigoriev A, Jegoulev V, Perrier S, and others. (2006) SPICAM
39 1353 IR acousto-optic spectrometer experiment on Mars Express. *J Geophys Res*,
40 1354 111, E09S03.
- 41 1355 Korablev OI, Kalinnikov YK, Titov AY, Rodin AV, Smirnov YV, Poluarshinov
42 1356 MA, Kostrova EA, Kalyuzhnyi AV, Trokhimovskii AY, Vinogradov II and
43
44
45
46
47
48
49
50
51
52
53
54
55
56
57
58
59
60

- 1
2
3
4
5
6
7 1357 others. (2011) The RUSALKA device for measuring the carbon dioxide and
8 1358 methane concentration in the atmosphere from on board the International
9 1359 Space Station. *J Optical Technol*, 78, 317-327.
10 1360 Korablev O, Fedorova A, Bertaux JL, Stepanov AV, Kiselev A, Kalinnikov YK,
11 1361 Titov AY, Montmessin F, Dubois JP, Villard E, and others. (2012) SPICAV
12 1362 IR acousto-optic spectrometer experiment on Venus Express. *Planet Space*
13 1363 *Sci*, 65, 38-57.
14 1364 Korablev O, Fedorova A, Villard E, Joly L, Kiselev A, Belyaev D, and Bertaux J-
15 1365 L. (2013) Characterization of the stray light in a space borne atmospheric
16 1366 AOTF spectrometer. *Optics Express*, 21, 18354.
17 1367 Korablev O, Trokhimovsky A, Grigoriev AV, Shakun A, Ivanov YS, Moshkin B,
18 1368 Anufreychik K, Timonin D, Dziuban I, Kalinnikov YK and others. (2014)
19 1369 Three infrared spectrometers, an atmospheric chemistry suite for the
20 1370 ExoMars 2016 trace gas orbiter. *J Appl Remote Sensing*, 8, 4983.
21 1371 Korablev O, Ivanov A, Fedorova A, Kalinnikov YK, Shapkin A, Mantsevich S,
22 1372 Viazovetsky N, Evdokimova N, and Kiselev AV. (2015) Development of a
23 1373 mast or robotic arm-mounted infrared AOTF spectrometer for surface Moon
24 1374 and Mars probes. *Proc SPIE*, 9608, 07-10.
25 1375 Lane, M.D, Mertzman, S.A, Dyar, M.D, and Bishop, J.L. (2011) Phosphate
26 1376 minerals measured in the visible-near infrared and thermal infrared: Spectra
27 1377 and XRD analysis. *LPI Contribution*, 1608, 1013.
28 1378 Leftwich, K, Bish, D.L, and Chen, C.H. (2013) Crystal structure and
29 1379 hydration/dehydration behavior of $\text{Na}_2\text{Mg}(\text{SO}_4)_2 \cdot 16\text{H}_2\text{O}$: A new hydrate
30 1380 phase observed under Mars-relevant conditions. *American Mineralogist*, 98,
31 1381 1772-1778.
32 1382 Lemmon MT, Wolff MJ, Smith MD, Clancy RT, Banfield D, Landis GA, Ghosh
33 1383 A, and others. (2004) Atmospheric imaging results from the Mars
34 1384 Exploration Rovers: Spirit and Opportunity. *Science*, 306, 1753.
35 1385 Leroi V, Bibring JP, and Berthe M. (2009) Micromega/IR: Design and status of a
36 1386 near-infrared spectral microscope for in situ analysis of Mars samples. *Planet*
37 1387 *Space Sci*, 57, 1068-1075.
38 1388 Manning CV, McKay CP, and Zahnle KJ. (2008) The nitrogen cycle on Mars:
39 1389 Impact decomposition of near-surface nitrates as a source for a nitrogen
40 1390 steady state. *Icarus*, 197, 60-64.
41
42
43
44
45
46
47
48
49
50
51
52
53
54
55
56
57
58
59
60

- 1
2
3
4
5
6
7 1391 Mantsevich SN, Korablev OI, Kalinnikov YK, Ivanov AY, and Kiselev AV.
8 1392 (2015) Wide-aperture TeO₂ AOTF at low temperatures: Operation and
9 1393 survival. *Ultrasonics*, 59, 50-58.
- 10 1394 Markiewicz WJ, Sablotny RM, Keller HU, Thomas N, Titov D, and Smith PH.
11 1395 (1999) Optical properties of the martian aerosols as derived from Imager for
12 1396 Mars Pathfinder midday sky brightness data. *J Geophys Res*, 104, 9009-9018.
- 13 1397 Marshall CP, Love GD, Snape CE, Hill AC, Allwood AC, Walter MR, Van
14 1398 Kranendonk MJ, Bowden SA, Sylva SP, and Summons RE. (2007) Structural
15 1399 characterization of kerogen in 3.4 Ga Archaean cherts from the Pilbara
16 1400 Craton, Western Australia. *Precambrian Research*, 155, 1-23.
- 17 1401 Martin-Torres FJ, Zorzano MP, Valentin-Serrano P, Harri AM, Genzer M,
18 1402 Kemppinen O, Rivera-Valentin EG, Jun I, Wray J, Bo Madsen M, and others.
19 1403 (2015) Transient liquid water and water activity at Gale crater on Mars.
20 1404 *Nature Geosci*, 8, 357-361.
- 21 1405 McKay DS, Gibson EK, Thomas-Keprta KL, Vali H, Romanek CS, Clemett SJ,
22 1406 Chillier XDF, Maechling CR, and Zare RN. (1996) Search for past life on
23 1407 Mars: Possible relic biogenic activity in martian meteorite ALH84001.
24 1408 *Science*, 273, 924-930.
- 25 1409 Milliken RE, and Mustard JF. (2005) Quantifying absolute water content of
26 1410 minerals using near-infrared reflectance spectroscopy. *J Geophys Res*, 110,
27 1411 E12001.
- 28 1412 Milliken RE, Mustard JF, Poulet F, Jouglet D, Bibring JP, Gondet B, and
29 1413 Langevin Y. (2007) Hydration state of the martian surface as seen by Mars
30 1414 Express OMEGA: 2. H₂O content of the surface. *J Geophys Res*, 112,
31 1415 E08S07.
- 32 1416 Morris RV, Ruff SW, Gellert R, Ming DW, Arvidson RE, Clark BC, Golden DC,
33 1417 Siebach K, Klingelhöfer G, Schröder C, and Fleischer I. (2010) Identification
34 1418 of carbonate-rich outcrops on Mars by the Spirit rover. *Science*, 329, 421-424.
- 35 1419 Murchie S, Arvidson R, Bedini P, Beisser K, Bibring J-P, Bishop J, Boldt J,
36 1420 Cavender P, Choo T, Clancy RT and others. (2007) Compact Reconnaissance
37 1421 Imaging Spectrometer for Mars (CRISM) on Mars Reconnaissance Orbiter
38 1422 (MRO). *J Geophys Res*, 112, E05S03.
- 39 1423 Murchie S, Roach L, Seelos F, Milliken R, Mustard J, Arvidson R, Wiseman S,
40 1424 Lichtenberg K, Andrews-Hanna J, Bishop J, and others. (2009) Evidence for
41 1425 the origin of layered deposits in Candor Chasma, Mars, from mineral
42 1426 composition and hydrologic modeling. *J Geophys Res*, 114, E00D05.

- 1
2
3
4
5
6
7 1427 Nachon M, Clegg SM, Mangold N, Schröder S, Kah LC, Dromart G, Ollila A,
8 1428 Johnson JR, Oehler DZ, Bridges JC, and others. (2014) Calcium sulfate veins
9 1429 characterized by ChemCam/Curiosity at Gale crater, Mars. *J Geophys Res*,
10 1430 119, 1991-2016.
- 11 1431 Navarro-González R, Stern J, Sutter B, Archer D, McAdam A, Franz HB, C. P.
12 1432 McKay CP, Coll P, Cabane M, Ming DW and others. (2013) Possible
13 1433 detection of nitrates on Mars by the Sample Analysis at Mars (SAM)
14 1434 instrument. *LPI Contribution*, 1719, 2648.
- 15 1435 Neefs E, Vandaele AC, Drummond R, Thomas IR, Berkenbosch S, Clairquin R,
16 1436 Delanoye S, Ristic B, Maes J, Bonnewijn S, and others. (2015) NOMAD
17 1437 spectrometer on the ExoMars trace gas orbiter mission: Part 1—design,
18 1438 manufacturing and testing of the infrared channels. *Applied Optics*, 54, 8494.
- 19 1439 Nevejans D, Neefs E, Van Ransbeeck E, Berkenbosch S, Clairquin R, De Vos L
20 1440 Moelans W, Glorieux S, Baeke A, Korablev O, and others. (2006) Compact
21 1441 high-resolution spaceborne echelle grating spectrometer with acousto-optical
22 1442 tunable filter based order sorting for the infrared domain from 2.2 to 4.3 μm .
23 1443 *Applied Optics*, 45, 5191-5206.
- 24 1444 Noe Dobrea EZ, McAdam AC, Freissinet C Franz H, Belmahdi I, Hammersley,
25 1445 MR, Stoker CR, Parker B, Ja Kim K, Glavin DP, Calef F, Aubrey AD (2016)
26 1446 Characterizing the mechanisms for the preservation of organics at the Painted
27 1447 Desert: Lessons for MSL, ExoMars, and Mars 2020. *LPI Contribution*, 1903,
28 1448 2796.
- 29 1449 Ody A, Poulet F, Langevin Y, Bibring JP, Bellucci G, Altieri F, Gondet B,
30 1450 Vincendon M, Carter J, and Manaud N. (2012) Global maps of anhydrous
31 1451 minerals at the surface of Mars from OMEGA/MEx. *J Geophys Res*, 117,
32 1452 E00J14.
- 33 1453 Ody A, Poulet F, Bibring JP, Loizeau D, Carter J, Gondet B, and Langevin Y.
34 1454 (2013) Global investigation of olivine on Mars: Insights into crust and mantle
35 1455 compositions. *J Geophys Res*, 118, 234-262.
- 36 1456 Ojha L, Wilhelm MB, Murchie SL, McEwen AS, Wray JJ, Hanley J, Massé M,
37 1457 and Chojnacki M. (2015) Spectral evidence for hydrated salts in recurring
38 1458 slope lineae on Mars. *Nature Geosci*, 8, 829-832.
- 39 1459 Osterloo MM, Anderson FS, Hamilton VE, and Hynek BM. (2010) Geologic
40 1460 context of proposed chloride-bearing materials on Mars. *J Geophys Res*,
41 1461 115, E10012.
- 42
43
44
45
46
47
48
49
50
51
52
53
54
55
56
57
58
59
60

- 1
2
3
4
5
6 1462 Palomba E, Zinzi A, Cloutis EA, D'Amore M, Grassi D, and Maturilli A (2009)
7 1463 Evidence for Mg-rich carbonates on Mars from a 3.9 μm absorption band.
8 1464 *Icarus*, 203, 58-65.
9
10 1465 Pilorget C, and Bibring JP. (2013) NIR reflectance hyperspectral microscopy for
11 1466 planetary science: Application to the MicrOmega instrument. *Planet Space*
12 1467 *Sci*, 76, 42-52.
13
14 1468 Poulet F, Bibring JP, Mustard JF, Gendrin A, Mangold N, Langevin Y, Arvidson
15 1469 RE, Gondet B, and Gomez C. (2005) Phyllosilicates on Mars and
16 1470 implications for early martian climate. *Nature*, 438, 623-627.
17
18 1471 Poulet F, Mangold N, Platevoet B, Bardintzeff JM, Sautter V, Mustard JF,
19 1472 Bibring JP, Pinet P, Langevin Y, Gondet B, and others. (2009) Quantitative
20 1473 compositional analysis of martian mafic regions using the MEx/OMEGA
21 1474 reflectance data: 2. Petrological implications. *Icarus*, 201, 84-101.
22
23 1475 Quinn RC, Chittenden JD, Kounaves SP, and Hecht MH. (2011) The oxidation-
24 1476 reduction potential of aqueous soil solutions at the Mars Phoenix landing site.
25 1477 *Geophys Res Lett*, 38, 14202.
26
27 1478 Rice MS, Bell III JF, Cloutis EA, Wray JJ, Herkenhoff KE, Sullivan R, Johnson
28 1479 JR, and Anderson RB. (2011) Temporal observations of bright soil exposures
29 1480 at Gusev crater, Mars. *J Geophys Res*, 116, E00F14.
30
31 1481 Rice MS, Cloutis EA, Bell III JF, Bish DL, Horgan BH, Mertzman SA, Craig MA,
32 1482 Renaut RW, Gautason B, and Mountain B. (2013) Reflectance spectra
33 1483 diversity of silica-rich materials: Sensitivity to environment and implications
34 1484 for detections on Mars. *Icarus*, 223, 499-533.
35
36 1485 Sefton-Nash E, Catling DC, Wood SE, Grindrod PM, and Teanby NA. (2012)
37 1486 Topographic, spectral and thermal inertia analysis of interior layered deposits
38 1487 in Iani Chaos, Mars. *Icarus*, 221, 20-42.
39
40 1488 Smith MD, Wolff MJ, Spanovich N, Ghosh A, Banfield D, Christensen PR,
41 1489 Landis GA, and Squyres SW. (2006) One martian year of atmospheric
42 1490 observations using MER Mini-TES. *J Geophys Res*, 111, E12S13.
43
44 1491 Smith MR, and Bandfield JL. (2012) Geology of quartz and hydrated silica-
45 1492 bearing deposits near Antoniadi Crater, Mars. *J Geophys Res*, 117, E06007.
46
47 1493 Smith MR, Bandfield JL, Cloutis EA, and Rice MS. (2013) Hydrated silica on
48 1494 Mars: Combined analysis with near-infrared and thermal-infrared
49 1495 spectroscopy. *Icarus*, 223, 633-648.
50
51 1496 Squyres SW, Arvidson RE, Bell JF, Brückner J, Cabrol NA, Calvin W, Carr MH,
52 1497 Christensen PR, Clark BC, Crumpler L, and others. (2004) The Opportunity
53
54
55
56
57
58
59
60

- 1
2
3
4
5
6
7 1498 rover's Athena science investigation at Meridiani Planum, Mars. *Science*, 306,
8 1499 1698-1703.
- 9 1500 Stephenson JD, Hallis LJ, Nagashima K, Freeland SJ. (2013) Boron enrichment in
10 1501 martian clay. *PLoS ONE*, 8(6), e64624.
- 11 1502 Titov DV, Markiewicz WJ, Thomas N, Keller HU, Sablotny RM, Tomasko MG,
12 1503 Lemmon MT, and Smith PH. (1999) Measurements of the atmospheric water
13 1504 vapor on Mars by the Imager for Mars Pathfinder. *J Geophys Res*, 104, 9019-
14 1505 9026.
- 15 1506 Vago JL, Lorenzoni L, Calantropio F, and Zashchirinskiy AM. (2015) Selecting a
16 1507 landing site for the ExoMars 2018 mission. *Solar System Res*, 49, 538-542.
- 17 1508 Vago J, Westall F, Coates A, Jaumann R, Korablev O, Ciarletti V, Mitrofanov I,
18 1509 Josset J-L, De Sanctis M, Bibring J-P, and others. (2017). Habitability on
19 1510 early Mars and the search for biosignatures with the Exo-Mars rover.
20 1511 *Astrobiology*, this issue
- 21 1512 Vincendon M, Pilorget C, Gondet B, Murchie S, and Bibring JP. (2011) New
22 1513 near-IR observations of mesospheric CO₂ and H₂O clouds on Mars. *J*
23 1514 *Geophys Res*, 116, E00J02.
- 24 1515 Wang A, Haskin LA, Squyres SW, Jolliff BL, Crumpler L, Gellert R, Schröder C,
25 1516 Herkenhoff K, Hurowitz J, Tosca NJ, and others. (2006) Sulfate deposition in
26 1517 subsurface regolith in Gusev crater, Mars. *J Geophys Res*, 111, E02S17.
- 27 1518 Wray JJ, Murchie SL, Bishop JL, Ehlmann BL, Milliken RE, Wilhelm MB,
28 1519 Seelos KD, and Chojnacki M. (2016) Orbital evidence for more widespread
29 1520 carbonate-bearing rocks on Mars. *J Geophys Res*, 121, 652-677.
- 30 1521 Zelenyi L, Mitrofanov I, Petrukovich A, Khartov V, Martynov M, and
31 1522 Lukianchikov A. (2014) Russian plans for lunar investigations. Stage 1.
32 1523 *European Planet Sci Congress 2014 9*, EPSC2014-702.
- 33 1524 Zorzano MP, Mateo-Martí E, Prieto-Ballesteros O, Osuna S, and Renno N. (2009)
34 1525 Stability of liquid saline water on present day Mars. *Geophys Res Lett*, 36,
35 1526 L20201.
- 36
37
38
39
40
41
42
43
44
45
46
47
48
49
50
51
52
53
54
55
56
57
58
59
60